

This is the author's peer reviewed, accepted manuscript. However, the online version of record will be different from this version once it has been copyedited and typeset.

PLEASE CITE THIS ARTICLE AS DOI: 10.1063/5.0100169

LES of Helical and Straight VAWTs in Boundary Layer Turbulence J. Renew. Sustain. Energy

<sup>1</sup> **Large Eddy Simulation of Helical- and Straight-Bladed Vertical Axis Wind Turbines  
in Boundary Layer Turbulence**

<sup>3</sup> Masoumeh Gharaati,<sup>1</sup> Shuolin Xiao,<sup>1,2</sup> Nathaniel J. Wei,<sup>3</sup> Luis A. Martínez-Tossas,<sup>4</sup>  
<sup>4</sup> John O. Dabiri,<sup>3,5</sup> and Di Yang<sup>\*1</sup>

<sup>5</sup> *Department of Mechanical Engineering, University of Houston, Houston, TX 77204,  
USA*

<sup>7</sup> *Current address: School of Civil and Environmental Engineering, Cornell University,  
Ithaca, NY 14853, USA.*

<sup>9</sup> *Graduate Aeronautical Laboratories, California Institute of Technology, Pasadena,  
CA 91125, USA*

<sup>11</sup> *National Renewable Energy Laboratory, Golden, CO 80401,  
USA*

<sup>13</sup> *Department of Mechanical and Civil Engineering, California Institute of Technology,  
Pasadena, CA 91125, USA*

<sup>15</sup> (\*Email address for correspondence: diyang@uh.edu)

<sup>16</sup> (Dated: 3 August 2022)

This is the author's peer reviewed, accepted manuscript. However, the online version of record will be different from this version once it has been copyedited and typeset.

PLEASE CITE THIS ARTICLE AS DOI: 10.1063/5.0100169

## LES of Helical and Straight VAWTs in Boundary Layer Turbulence

17 Turbulent wake flows behind helical-bladed and straight-bladed vertical axis wind turbines  
18 (VAWTs) in atmospheric boundary layer are studied numerically using the large-eddy sim-  
19 ulation (LES) method combined with the actuator line model. Based on the LES data,  
20 systematic statistical analysis are performed to explore the effects of blade geometry on  
21 the characteristics of the turbine wake. The time-averaged velocity fields show that the  
22 helical-bladed VAWT generates a mean vertical velocity along the center of the turbine  
23 wake, which causes a vertical inclination of the turbine wake and alters the vertical gra-  
24 dient of the mean streamwise velocity. Consequently, the intensities of the turbulent fluc-  
25 tuations and Reynolds shear stresses are also affected by the helical-shaped blades when  
26 compared with those in the straight-bladed VAWT case. The LES results also show that  
27 reversing the twist direction of the helical-bladed VAWT causes the spatial patterns of the  
28 turbulent wake flow statistics to be reversed in the vertical direction. Moreover, the mass  
29 and kinetic energy transports in the turbine wakes are directly visualized using the trans-  
30 port tube method, the comparison between the helical- and straight-bladed VAWT cases  
31 show significant differences in the downstream evolution of the transport tubes.

## LES of Helical and Straight VAWTs in Boundary Layer Turbulence

### **32 I. INTRODUCTION**

33 Vertical-axis wind turbines (VAWTs) and horizontal-axis wind turbines (HAWTs) are the two  
34 main types of wind-energy extraction devices.<sup>1,2</sup> HAWTs have proven themselves to be an effec-  
35 tive energy-harvesting technology over the past several decades and are widely used in most com-  
36 mercial wind farms today in both onshore and offshore contexts.<sup>2–5</sup> Modern commercial HAWTs  
37 can produce megawatts of power with high power-conversion efficiencies.<sup>2,6</sup> Despite their com-  
38 mercial success, the large size of HAWTs (whose rotor diameters are often in excess of 100 meters)  
39 creates some logistical difficulties. Aerodynamically, the optimal spacing in the streamwise direc-  
40 tion of HAWTs in a wind farm may be as much as 15 diameters or larger,<sup>7</sup> which translates to large  
41 amounts of land or offshore water area required for effective operation and correspondingly lower  
42 wind-farm power densities. The size of HAWT blades and towers also creates logistical difficul-  
43 ties for construction, transport, and maintenance.<sup>8</sup> Additionally, HAWTs must face the incoming  
44 wind for optimal power production, necessitating complex yaw-control schemes to compensate  
45 for changing wind direction.<sup>9</sup>

46 VAWTs, on the other hand, have wakes that recover relatively quickly, in some cases within 6  
47 turbine diameters downstream.<sup>10</sup> They can thus be placed in closely packed arrays for improved  
48 wind-farm power densities. Furthermore, VAWTs placed in close proximity to each other can  
49 mutually benefit from aerodynamic interactions for improved overall efficiencies.<sup>11,12</sup> The perfor-  
50 mance of a VAWT is insensitive to wind direction, eliminating the need for yaw-control systems.  
51 VAWTs also typically have smaller diameters and their electrical components may be mounted  
52 closer to the ground for ease of operations and maintenance. Finally, VAWTs tend to operate  
53 at lower TSRs than HAWTs and thus may generate less noise.<sup>13,14</sup> For these reasons, VAWTs  
54 represent a potential wind-energy solution for contexts in which traditional HAWT farms are im-  
55 practical or infeasible, such as sites with limited land area or frequently changing wind direction.

56 Unlike HAWTs, whose designs are relatively uniform, there exist several different types of  
57 VAWT designs that are distinguished by their blade geometries, including Savonius turbines, Dar-  
58 rrieus turbines with curved blades, straight-bladed Darrieus turbines, and helical-bladed Darrieus  
59 turbines.<sup>13</sup> Among these different types, the straight-bladed VAWTs have been studied and de-  
60 ployed more frequently due to their relatively simple blade geometry.<sup>12,14–22</sup> A number of labo-  
61 ratory experiments have been conducted to gain fundamental understanding of the VAWT wake  
62 flows under uniform mean inflow conditions.<sup>12,15–17,19,20,23</sup> Several field experiments have also

## LES of Helical and Straight VAWTs in Boundary Layer Turbulence

been performed to study the interactions of straight-bladed VAWTs with turbulent wind in the atmospheric boundary layer (ABL), which have provided crucial information for assessing the performance of VAWTs in realistic environments.<sup>10,11,18,22</sup>

In recent years, helical-bladed VAWTs have begun to attract more attention due to several potential advantages, such as a low cut-in wind speed, low temporal oscillations in torque and power, and low noise level.<sup>24–27</sup> Several numerical studies have used the unsteady Reynolds averaged Navier–Stokes (URANS) modeling approach to study the aerodynamic performance and power production of helical-bladed VAWTs in comparison with straight-bladed VAWTs.<sup>25–28</sup> Wei *et al.*<sup>22</sup> performed field experiments using three-dimensional particle-tracking velocimetry to measure the time-averaged velocities and vorticities downstream of a full-scale helical-bladed VAWT and compared its near-wake flow structures with those downstream of a straight-bladed VAWT. Despite these recent advances, our current understanding of the wake characteristics of helical-bladed VAWTs is still limited with respect to straight-bladed VAWTs. For potential applications in large-scale commercial VAWT farms, it is crucial to understand the characteristics of the wake flows behind helical-bladed VAWTs, such as the mean wind-speed recovery, turbulence intensity, and mass and energy exchanges between the low-speed wake flow and the high-speed surrounding flow, which are important for assessing the impact of upstream turbines on the performance of downstream turbines in large turbine arrays.<sup>6,21,29–34</sup>

In recent years, large-eddy simulation (LES) has become a promising tool for modeling the turbulent flow dynamics in the turbine wake flows and in the turbine array boundary layers (i.e., in large wind farms).<sup>30,35–38</sup> In particular, LES equipped with the actuator line model (ALM) for wind turbines has shown successful applications in modeling HAWTs and VAWTs wake flows.<sup>14,37–48</sup> Several recent LES studies on straight-bladed VAWTs have provided valuable insights for understanding the characteristics of the turbine wake flows under various laboratory and ABL flow conditions. In this study, we adopt the Johns Hopkins University LES model, LESGO, as the main wind turbulence solver.<sup>49</sup> LESGO is equipped with an ALM module implemented originally for modeling HAWTs.<sup>37,41,42,50</sup> This existing ALM module is modified in the present study to model the straight-bladed and helical-bladed VAWTs.

The present work aims to study the effects of blade geometry on the wake flow characteristics of VAWTs. To this end, three VAWTs with different blade geometries are considered: one straight-bladed VAWT and two helical-bladed VAWTs with opposite blade twist directions but the same twist rate of  $39.69^\circ/m$  along the vertical direction. The straight-bladed VAWT can be regarded

## LES of Helical and Straight VAWTs in Boundary Layer Turbulence

95 as a special version of the helical-bladed VAWT with zero blade twist angle. These three VAWTs  
 96 have identical parameters, including the rotor equator height (8.2 m), rotor diameter (1.8 m), blade  
 97 vertical length (3.2 m), and blade cross-sectional geometry. A concurrent precursor simulation  
 98 method is used to generate realistic boundary layer turbulence inflow condition with a mean wind  
 99 speed of 11.79 m/s at the VAWT equator height. Based on statistically identical inflow conditions,  
 100 the interactions of the three different VAWTs with the boundary layer turbulence are simulated  
 101 using the LES model. The TSR for VAWT rotation is kept the same at 1.19 for all three VAWT  
 102 cases to allow direct comparison of the simulation results. The key VAWT parameters, wind speed,  
 103 and TSR value are chosen to match the field experiments of Wei *et al.*<sup>22</sup> Based on the LES data,  
 104 the effects of the helical-shaped blades on the characteristics of the turbulent wake flows are sys-  
 105 tematically investigated by direct observations of the instantaneous velocities, comparison of the  
 106 time-averaged velocities, as well as analysis of the statistics of the turbulent velocity fluctuations  
 107 in the turbine wake region.

108 The remainder of this paper is organized as follows. The LES model for wind turbulence  
 109 and the actuator line model for the VAWT are introduced in Sec. II. In Sec. III, two test cases  
 110 based on straight-bladed VAWTs are provided to validate the current LES model. In Sec. IV, the  
 111 LES cases for studying the effects of helical-bladed VAWTs on the wake flow characteristics are  
 112 presented in detail, including the case configurations, the instantaneous flow fields, and the time-  
 113 averaged mean-flow and turbulent-fluctuation statistics. Finally, the implications of these results  
 114 are discussed in Sec. V.

## 115 II. NUMERICAL METHOD FOR WIND TURBULENCE AND TURBINE MODEL

### 116 A. Large-eddy simulation of wind turbulence

117 In this study, we perform simulations of helical- and straight-bladed VAWTs interacting with  
 118 fully developed wind turbulence in a neutral boundary layer. We adopt the large-eddy simula-  
 119 tion model LESGO developed by the Turbulence Research Group at Johns Hopkins University as  
 120 the main wind turbulence solver.<sup>49</sup> The wind turbulent flow motions are governed by the three-  
 121 dimensional incompressible filtered Navier–Stokes equations

$$122 \quad \nabla \cdot \tilde{\mathbf{u}} = 0, \quad (1)$$

$$123 \quad \frac{\partial \tilde{\mathbf{u}}}{\partial t} + \nabla \cdot (\tilde{\mathbf{u}} \tilde{\mathbf{u}}) = -\frac{1}{\rho} \nabla \tilde{p} + \nu \nabla^2 \tilde{\mathbf{u}} - \nabla \cdot \boldsymbol{\tau} + \frac{\mathbf{f}_x}{\rho} - \frac{\tilde{\mathbf{f}}_e}{\rho}. \quad (2)$$

## LES of Helical and Straight VAWTs in Boundary Layer Turbulence

124 Here, the tilde denotes filtering at the LES grid scale  $\Delta$ ;  $\tilde{\mathbf{u}} = (\tilde{u}, \tilde{v}, \tilde{w})$  is the resolved flow velocity  
 125 vector, where  $\tilde{u}$ ,  $\tilde{v}$  and  $\tilde{w}$  are the corresponding components in the streamwise ( $x$ ), spanwise ( $y$ ),  
 126 and vertical ( $z$ ) directions, respectively;  $\nu$  is the kinematic viscosity of air;  $\rho$  is the air density;  $\tilde{p}$   
 127 is the resolved pressure;  $\boldsymbol{\tau} = \tilde{\mathbf{u}}\tilde{\mathbf{u}} - \tilde{\mathbf{u}}\tilde{\mathbf{u}}$  is the subgrid-scale (SGS) stress tensor;  $\mathbf{f}_x$  is an imposed  
 128 streamwise body force to drive the wind turbulence; and  $\tilde{\mathbf{f}}_e$  is a distributed body force for modeling  
 129 the effect of the wind turbine on the flow. More details about  $\mathbf{f}_x$  and  $\tilde{\mathbf{f}}_e$  are given below.

130 To close Eq. (2), the deviatoric part of the SGS stress tensor  $\boldsymbol{\tau}^d$  is parameterized using the  
 131 eddy-viscosity type model,<sup>51,52</sup>  $\boldsymbol{\tau}^d = -2\nu_\tau \tilde{\mathbf{S}} = -2(c_s\Delta)^2 |\tilde{\mathbf{S}}| \tilde{\mathbf{S}}$ , where  $\nu_\tau$  is the SGS eddy viscosity,  
 132  $c_s$  is the Smagorinsky coefficient,  $\tilde{\mathbf{S}} = [\nabla \tilde{\mathbf{u}} + (\nabla \tilde{\mathbf{u}})^T]/2$  is the resolved strain rate tensor, and  
 133  $|\tilde{\mathbf{S}}| \equiv \sqrt{2\tilde{\mathbf{S}} : (\tilde{\mathbf{S}})^T}$  is the magnitude of  $\tilde{\mathbf{S}}$ . The trace of the SGS stress tensor  $\text{tr}(\boldsymbol{\tau})$  is not modeled ex-  
 134 plicitly, but instead is absorbed into the pressure term as commonly done in LES of incompressible  
 135 turbulence.<sup>52–55</sup> In LESGO, the instantaneous local value of  $c_s$  is calculated dynamically during  
 136 the simulation using the Lagrangian-averaged scale-dependent dynamic (LASD) SGS model.<sup>56</sup>  
 137 LES utilizing the LASD model has been used in a number of prior studies on wind-turbine wake  
 138 flows.<sup>30,35,36,57–59</sup>

139 A concurrent precursor method is used to provide the fully developed neutral boundary layer  
 140 turbulence inflow condition for modeling the wind–VAWT interaction.<sup>60</sup> As shown in Fig. 1, the  
 141 overall simulation domain consists of two sub-domains that are computed simultaneously in the  
 142 LES, i.e., the precursor simulation domain for fully developed boundary layer turbulence without  
 143 VAWTs and the main simulation domain for turbulence interacting with VAWTs. The precursor  
 144 simulation uses periodic boundary conditions in the  $x$ - and  $y$ -directions, and the mean flow is  
 145 driven by a constant pressure gradient imposed in the  $x$ -direction,<sup>30,36,60</sup>

$$146 \quad \mathbf{f}_x = -\frac{dp_\infty}{dx} \hat{\mathbf{e}}_x, \quad (3)$$

147 where  $\hat{\mathbf{e}}_x$  is the unit vector in the  $x$ -direction. The turbine-induced force is set to  $\tilde{\mathbf{f}}_e = 0$  in the pre-  
 148 cursor domain. Different from the precursor simulation, the main simulation with the VAWTs uses  
 149 the inflow–outflow conditions in the  $x$ -direction and the periodic condition in the  $y$ -direction. The  
 150 fully developed boundary layer inflow condition extracted from the precursor simulation domain is  
 151 fed into the upstream end of the main simulation domain to push the wind turbulence through the  
 152 simulation domain towards the outflow boundary at the downstream end of the main simulation  
 153 domain. Associated with these inflow–outflow streamwise boundary conditions, the streamwise  
 154 body force  $\mathbf{f}_x$  is set to be zero in the main simulation domain. The turbine-induced force  $\tilde{\mathbf{f}}_e$  is

## LES of Helical and Straight VAWTs in Boundary Layer Turbulence

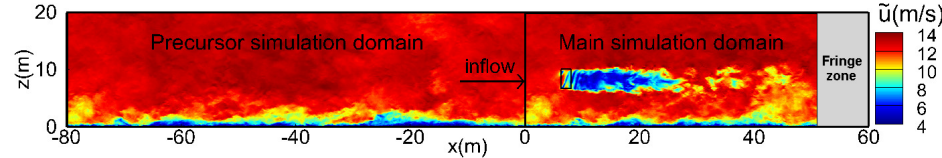


FIG. 1. Illustration of concurrent precursor method for modeling VAWT in boundary layer turbulence.

modeled using the actuator line model, which is discussed in Sec. II B.

The LESGO model uses the Fourier-series-based pseudo-spectral method for the spatial discretizations in the  $x$ - and  $y$ -directions. In order to use the inflow–outflow condition properly in a pseudo-spectral flow solver, the fringe-zone method is used for the main simulation.<sup>61,62</sup> As shown in Fig. 1, a fringe zone of finite streamwise length  $L_{fr}$  adjacent to the outflow boundary is used to achieve a smooth transition of the simulated wind turbulence in the far wake of the turbines back to its imposed value at the inflow boundary, which allows the simulation of the non-periodic turbine wake flows using the periodic pseudo-spectral flow solver. Specifically, in the fringe zone,  $x_{fr} \leq x \leq L_x$ , the flow velocity vector is imposed as

$$\tilde{\mathbf{u}}(x, y, z) = \tilde{\mathbf{u}}(x_{fr}, y, z) [1 - \psi(x)] + \tilde{\mathbf{u}}_{in}(y, z) \psi(x), \quad (4)$$

where  $L_x$  is the streamwise length of the main simulation domain,  $x_{fr} = L_x - L_{fr}$  is the streamwise location where the fringe zone starts,  $\psi(x) = 0.5 - 0.5 \cos [\pi(x - x_{fr})/L_{fr}]$  is the fringe function, and  $\tilde{\mathbf{u}}_{in}(y, z)$  is the inflow velocity for the main simulation provided by the precursor simulation (i.e., extracted at the downstream end of the precursor simulation domain as shown in Fig. 1). As illustrated in Fig. 2, this concurrent precursor method allows physical boundary layer turbulence inflow conditions to be obtained and used for modeling the VAWT wake flow. Details about the implementation of the concurrent precursor LES are provided in Secs. III B and IV A.

### B. Actuator line model for vertical axis wind turbines

In the current LES model, the aerodynamic forces induced by the turbine blades to the wind turbulence are computed using the ALM.<sup>39</sup> Let  $R$  be the radius of the VAWT rotor (i.e., the radial distance from the chord of the blade to the center axis of the VAWT),  $D = 2R$  be the turbine rotor diameter, and  $H$  be the vertical height of the blade. Each VAWT blade is discretized into  $N_b$  elements, with a vertical height of  $\Delta H = H/N_b$  for each blade element. For each blade element, the

LES of Helical and Straight VAWTs in Boundary Layer Turbulence

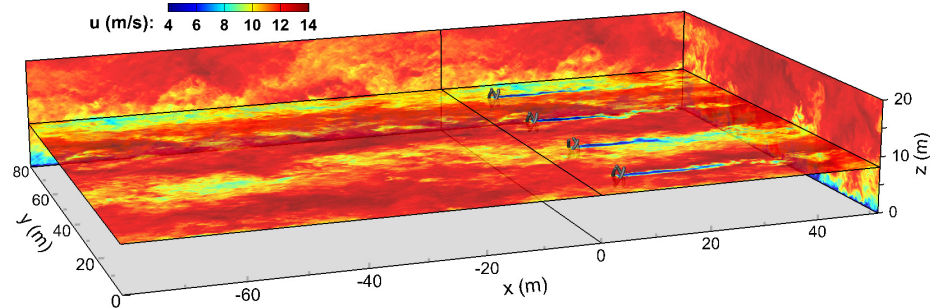


FIG. 2. Illustration of the three-dimensional flow field obtained from the current LES model. Color contours of the instantaneous streamwise velocity are shown on the domain walls and on the horizontal plane at the equator height of the VAWTs, which are shown in grey.

178 local relative velocity vector of the wind with respect to the element in the local  $(s, n)$  coordinate  
179 system is

$$180 \quad \mathbf{V}_{\text{rel}} = \mathbf{V}_{\text{local}} - R\Omega \hat{\mathbf{e}}_s. \quad (5)$$

181 As illustrated in Fig. 3,  $s$  and  $n$  are the local coordinates along the tangential and radial directions  
182 of the turbine blade element, respectively;  $\mathbf{V}_{\text{local}}$  is the local incoming wind velocity around the  
183 blade element projected to the  $(x, y)$ -plane through the center of the blade element;  $\Omega$  is the angular  
184 velocity of the VAWT rotation; and  $\hat{\mathbf{e}}_s$  is the unit vector along the tangential direction  $s$ .

185 The local wind velocity vector defined in the local  $(s, n)$  coordinate system can be written as

$$186 \quad \mathbf{V}_{\text{local}} = \tilde{U}_h \sin(\theta - \beta) \hat{\mathbf{e}}_s - \tilde{U}_h \cos(\theta - \beta) \hat{\mathbf{e}}_n, \quad (6)$$

187 where  $\hat{\mathbf{e}}_n$  is the unit vector in the radial direction  $n$ ,  $\theta$  is the azimuthal angle for the blade rotation,  
188  $\beta = \arctan(\tilde{v}/\tilde{u})$  is the horizontal directional angle of the inflow wind velocity, and  $\tilde{U}_h = \sqrt{\tilde{u}^2 + \tilde{v}^2}$   
189 is the magnitude of the sampled horizontal velocity. In the current model,  $\theta = 0$  when the blade  
190 element is located at the most upstream location (i.e., when the radial direction is aligned with the  
191  $-x$ -direction), and  $\theta$  increases when the blade rotates counterclockwise. Based on the direction of  
192  $\mathbf{V}_{\text{rel}}$ , the local angle of attack  $\alpha$  is calculated as

$$193 \quad \alpha = \arctan \left( \frac{-\cos(\theta - \beta)}{-\sin(\theta - \beta) + R\Omega/\tilde{U}_h} \right). \quad (7)$$

194 For a stationary or slowly moving airfoil, the lift and drag forces can be calculated using the  
195 static lift coefficient  $C_L$  and drag coefficient  $C_D$ , respectively, based on the values of  $\mathbf{V}_{\text{rel}}$  and  $\alpha$ .

LES of Helical and Straight VAWTs in Boundary Layer Turbulence

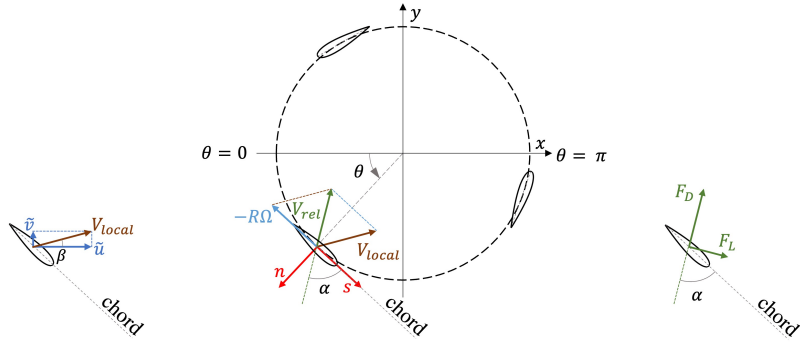


FIG. 3. Schematics of the physical quantities involved in the modeling of the VAWT blade forces.

196 However, VAWT blades rotating in turbulent wind can experience rapid changes in angle of attack,  
 197 resulting in a flow phenomenon called dynamic stall.<sup>63</sup> In order to model the aerodynamic forces  
 198 of the VAWT blades accurately, the modified Boeing–Vertol model<sup>64</sup> is used in the current LES  
 199 model as a dynamic-stall correction. Specifically, the modified angles of attack for the lift and  
 200 drag coefficients are modeled as

$$201 \quad \alpha_L^* = \alpha - \gamma_L \kappa \left( \left| \frac{c \dot{\alpha}}{2V_{rel}} \right| \right)^{\frac{1}{2}} \frac{\dot{\alpha}}{|\dot{\alpha}|}, \quad (8)$$

$$202 \quad \alpha_D^* = \alpha - \gamma_D \kappa \left( \left| \frac{c \dot{\alpha}}{2V_{rel}} \right| \right)^{\frac{1}{2}} \frac{\dot{\alpha}}{|\dot{\alpha}|}, \quad (9)$$

203 where  $c$  is the blade chord length,  $\dot{\alpha} = d\alpha/dt$  is the instantaneous rate of change of  $\alpha$ , and  $V_{rel}$   
 204 is the magnitude of the relative velocity vector  $\mathbf{V}_{rel}$ . The dimensionless model coefficients  $\gamma_L$ ,  $\gamma_D$   
 205 and  $\kappa$  are expressed as

$$206 \quad \gamma_L = 1.4 - 6 \left( 0.06 - \frac{t_b}{c} \right), \quad (10)$$

$$207 \quad \gamma_D = 1 - 2.5 \left( 0.06 - \frac{t_b}{c} \right), \quad (11)$$

$$208 \quad \kappa = 0.75 + 0.25 \frac{\dot{\alpha}}{|\dot{\alpha}|}, \quad (12)$$

209 where  $t_b$  is the blade thickness. Based on  $\alpha_L^*$  and  $\alpha_D^*$ , the lift and drag coefficients with the dynamic  
 210 stall correction can be computed as<sup>64</sup>

$$211 \quad C_L^* = \left( \frac{\alpha}{\alpha_L^* - \alpha_0} \right) C_L(\alpha_L^*), \quad (13)$$

$$212 \quad C_D^* = C_D(\alpha_D^*), \quad (14)$$

## LES of Helical and Straight VAWTs in Boundary Layer Turbulence

213 where  $\alpha_0$  is the angle of zero lift which is equal to 0 for symmetric airfoils. In the current LES  
 214 model, the static lift coefficient  $C_L$  and drag coefficient  $C_D$  are obtained directly from the tabulated  
 215 empirical data reported in Sheldahl and Klimas.<sup>65</sup> By projecting the lift and drag forces onto the  
 216  $x$ - and  $y$ -directions, the aerodynamics force vector acting on the  $k$ -th element of a VAWT blade is  
 217  $\mathbf{F}_k = F_{k,x}\hat{\mathbf{e}}_x + F_{k,y}\hat{\mathbf{e}}_y$ , where  $\hat{\mathbf{e}}_y$  is the unit vector in the  $y$ -direction,

$$218 \quad F_{k,x} = -\frac{1}{2}\rho V_{rel}^2 c \Delta H [C_L^* \cos(\theta + \alpha) + C_D^* \sin(\theta + \alpha)] , \quad (15)$$

$$219 \quad F_{k,y} = \frac{1}{2}\rho V_{rel}^2 c \Delta H [-C_L^* \sin(\theta + \alpha) + C_D^* \cos(\theta + \alpha)] . \quad (16)$$

220 To avoid numerical instability and reduce sensitivity to the grid size when applying the aerody-  
 221 namic force,  $\mathbf{F}_k$  is usually distributed smoothly on the grid points around the blade element instead  
 222 of at the center of the element.<sup>14,39,44,66</sup> In the current LES model, a three-dimensional Gaussian  
 223 kernel method<sup>39,41-43</sup> is adopted to distribute the aerodynamic force as

$$224 \quad \tilde{\mathbf{f}}_\varepsilon(x, y, z) = \sum_{k=1}^{N_b} \mathbf{F}_k G_k(x, y, z) , \quad (17)$$

225 where

$$226 \quad G_k(x, y, z) = \frac{1}{\varepsilon^3 \pi^{3/2}} \exp\left(-\frac{r_k^2}{\varepsilon^2}\right) \quad (18)$$

227 is the Gaussian kernel function,  $\varepsilon$  is the kernel width, and  $r_k = \sqrt{(x - x_k)^2 + (y - y_k)^2 + (z - z_k)^2}$  is  
 228 the distance between a space point  $(x, y, z)$  and the center point of the  $k$ -th blade element  $(x_k, y_k, z_k)$ .  
 229 The distributed force  $\tilde{\mathbf{f}}_\varepsilon$  calculated based on Eq. (17) is used in Eq. (2) to model the effect of turbine  
 230 on the air flow.

### 231 C. Numerical Methods

232 In the current LES model, the governing equations (1) and (2) are discretized by a Fourier-  
 233 series-based pseudo-spectral method on collocated grids in the  $x$ - and  $y$ -directions, and a second-  
 234 order central-difference method on staggered grids in the  $z$ -direction. For the basic LES flow  
 235 solver, periodic boundary conditions are used in the  $x$ - and  $y$ -directions, a local law-of-the-wall  
 236 condition is applied at the bottom boundary,<sup>53,56</sup> and a stress-free condition is imposed at the  
 237 top of the boundary. The momentum equation (2) is formulated and discretized in the rotational  
 238 form to provide conservation of mass and kinetic energy.<sup>67-69</sup> The 3/2 rule is used to eliminate  
 239 the aliasing error associated with the pseudo-spectral discretization of the convective terms.<sup>70</sup> The

## LES of Helical and Straight VAWTs in Boundary Layer Turbulence

240 governing equations are integrated in time using a fractional-step method consisting of a prediction  
241 step and a correction step. In particular, in the prediction step the velocity field is advanced in time  
242 by integrating Eq. (2) using the second-order Adams–Bashforth scheme, which yields a predicted  
243 velocity field. Then a Poisson equation is constructed based on the divergence-free constraint (1)  
244 for the new time step and is solved to obtain the pressure field. Using the gradient of the pressure,  
245 the predicted velocity field is projected to the divergence-free space to obtain the velocity field for  
246 the new time step. The above process repeats at every time step in the simulation to advance the  
247 flow field in time in LES. More details of numerical schemes used in the LES model can be found  
248 in Albertson<sup>71</sup> and Albertson and Parlange.<sup>69</sup>

### 249 III. MODEL VALIDATION

250 To validate the current LES-ALM model, we consider two different test cases. In the first  
251 test case, the LES model is applied to simulate the wake flow behind a laboratory-scale straight-  
252 bladed VAWT to reproduce the towing-tank experiment of Bachant and Wosnik.<sup>16</sup> In the second  
253 test case, the LES model is used to simulate the interaction between a straight-bladed VAWT and  
254 ABL turbulence to reproduce the LES results reported in Shamsoddin and Porté-Agel.<sup>38</sup> Details  
255 of these two validation cases are presented in the following two subsections.

#### 256 A. Towing-Tank Experiment Validation Case

257 The first validation case is designed to match the parameters of the towing-tank experiment  
258 in Bachant and Wosnik.<sup>16</sup> The VAWT in this case consists of three straight blades with a cross-  
259 sectional profile of a NACA0020 airfoil, as well as a cylindrical center mast with a diameter  
260 of  $D_{cm} = 0.095$  m. Each blade has a vertical height of  $H = 1$  m, a chord length of  $c = 0.14$  m,  
261 and a radial distance of  $R = D/2 = 0.5$  m to the center axis of the VAWT. The dimensions of  
262 the simulation domain in the  $x$ -,  $y$ - and  $z$ -directions are  $L_x = 7.2$  m =  $7.2D$ ,  $L_y = 3.7$  m =  $3.7D$ ,  
263 and  $L_z = 2.7$  m =  $2.7D$ , respectively. The inflow has a uniform streamwise mean velocity of  
264  $U_0 = 1$  m/s, and both the top and bottom boundaries are set to be free-slip to be compatible with  
265 this uniform inflow condition. The VAWT rotates counterclockwise at an angular speed of  $\Omega =$   
266  $3.8\text{ s}^{-1}$ , which yields a turbine tip-speed ratio (TSR) of  $\lambda = R\Omega/U_0 = 1.9$ . The corresponding  
267 turbine rotor Reynolds number is  $Re_D = U_0 D / v_w = 10^6$  and the blade chord Reynolds number<sup>16</sup>

## LES of Helical and Straight VAWTs in Boundary Layer Turbulence

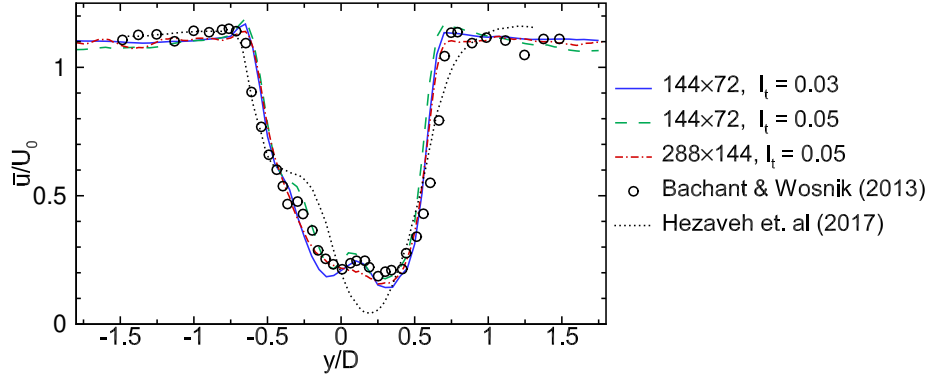


FIG. 4. Comparison of the spanwise profiles of the mean streamwise velocity at  $(x - x_0) = 1D$  for the towing tank validation case, where  $x_0$  is the streamwise location of the VAWT center axis. The towing tank experimental data points from Bachant and Wosnik<sup>16</sup> are denoted by the open circles. The LES result from Hezaveh *et al.*<sup>14</sup> obtained using  $288 \times 144 \times 60$  grid points is denoted by the dotted line (black). The results obtained from the current LES model are denoted as follows: solid line (blue) for  $I_t = 0.03$  with  $144 \times 72 \times 61$  grid points; dashed line (green) for  $I_t = 0.05$  with  $144 \times 72 \times 61$  grid points; dash-dot line (red) for  $I_t = 0.05$  with  $288 \times 144 \times 61$  grid points.

268 is  $Re_c = \lambda U_0 c / \nu_w = 2.66 \times 10^5$ , where the kinematic viscosity of water is  $\nu_w = 1.0 \times 10^{-6} \text{ m}^2/\text{s}$   
269 at 20°C.

270 The isotropic homogeneous turbulence dataset in the Johns Hopkins Turbulence Databases  
271 (JHTDB) is used to generate the turbulence fluctuations for the inflow condition based on the  
272 method developed by Martínez-Tossas *et al.*<sup>50</sup> Two different turbulent intensities are considered:  
273  $I_t \equiv \sqrt{2k/3}/U_0 = 0.03$  and  $0.05$ , where  $k = 0.5[(u'_{rms})^2 + (v'_{rms})^2 + (w'_{rms})^2]$  is the turbulent kinetic  
274 energy with  $(u'_{rms}, v'_{rms}, w'_{rms})$  being the root-mean-square (rms) values for the fluctuations of the  
275 inflow velocity components. For the test run with  $I_t = 0.05$ , two different grid resolutions are  
276 considered: a lower resolution with  $144 \times 72 \times 61$  grid points and a higher resolution with  $288 \times$   
277  $144 \times 61$  grid points. For the test run with  $I_t = 0.03$ , only the lower resolution with  $144 \times 72 \times 61$   
278 grid points is considered. These grid resolutions are chosen based on the LES tests of the same  
279 towing-tank experiment reported in Hezaveh *et al.*<sup>14</sup> For all three test cases, the width of the  
280 Gaussian kernel for the ALM is set to be  $\varepsilon = 0.1 \text{ m}$  for the VAWT blades and  $\varepsilon_{cm} = 0.05 \text{ m}$  for the  
281 center mast.

## LES of Helical and Straight VAWTs in Boundary Layer Turbulence

282 Figure 4 shows the comparison of the spanwise profiles of the time-averaged streamwise ve-  
283 locity at  $1D$  downstream of the VAWT. The time average of the current LES results is computed  
284 based on 2000 instantaneous snapshots of the flow field sampled between  $t = 24\text{s}$  and  $72\text{s}$ . The  
285 time-averaged velocity profiles of all three test runs obtained using the current LES model show  
286 good agreement with the experimental data.<sup>16</sup> The current LES results agree with the LES re-  
287 sult of Hezaveh *et al.*<sup>14</sup> for the overall magnitude and shape of the VAWT wake, but show some  
288 discrepancy in the detailed wake profile in  $-0.5 < y/D < 0.5$ . This discrepancy may be caused  
289 by several differences in the details of simulation setups. For example, in Hezaveh *et al.*<sup>14</sup> the  
290 turbine-induced forces were distributed equally over five points spanning the chord length and  
291 further distributed to additional surrounding points with constant prescribed weights, while the  
292 current LES model uses a 3D Gaussian kernel to smoothly distribute the forces. Moreover, the  
293 Reynolds number used in the current LES matches with that reported in Bachant and Wosnik,<sup>16</sup>  
294 while Hezaveh *et al.*<sup>14</sup> used a chord Reynolds number of  $Re_c = \lambda U_0 c / v_w = 5.7 \times 10^5$ , which is  
295 about twice of the value reported in Bachant and Wosnik.<sup>16</sup> It is also unclear if the cylindrical  
296 center mast of the VAWT was considered in the LES of Hezaveh *et al.*<sup>14</sup> Nevertheless, the cur-  
297 rent LES results show overall good agreement with the experimental and LES data reported in the  
298 literature and low sensitivity to the grid resolution.

299 Note that the specific value of the inflow turbulence intensity was not reported in Hezaveh  
300 *et al.*<sup>14</sup> and Bachant and Wosnik.<sup>16</sup> As a reference, Shamsoddin and Porté-Agel<sup>40</sup> and Abkar  
301 and Dabiri<sup>44</sup> performed LES of VAWT wake flow in water channel at a higher TSR of  $\lambda = 3.85$   
302 using an inflow turbulence intensity of 0.03. The two inflow turbulence intensities used in our  
303 LES model for the validation case are similar to that used in Shamsoddin and Porté-Agel<sup>40</sup> and  
304 Abkar and Dabiri.<sup>44</sup> As shown by the comparison in Fig. 4, the current LES model results are  
305 not sensitive to the choice of inflow turbulence intensity and both test cases (i.e.,  $I_t = 0.03$  with  
306  $144 \times 72 \times 61$  grid points) show good agreement with the reported experimental data. Note that  
307 if an even higher value of  $I_t$  is used for inflow, the stronger turbulent mixing of the inflow would  
308 enhance the wake recovery and also make the wake profile smoother. Nevertheless, considering  
309 the relatively low Reynolds number of the experiment in Bachant and Wosnik,<sup>16</sup> the relatively low  
310 turbulence intensities of  $I_t = 0.03$  and 0.05 appear to be more reasonable choices for the current  
311 validation case than other higher values.

## LES of Helical and Straight VAWTs in Boundary Layer Turbulence

### 312 B. Atmospheric Boundary Layer Flow Validation Case

313 The second validation case is configured based on the LES study of wind–VAWT interac-  
314 tion in a neutral ABL as reported in Shamsoddin and Porté-Agel.<sup>38</sup> In this case, the VAWT  
315 consists of three straight blades with the cross-sectional shape of the NACA0018 airfoil. Each  
316 blade has a vertical height of  $H = 100$ m and a chord length of  $c = 2.4$ m. The turbine ro-  
317 tor diameter is  $D = 2R = 50$ m, and the rotor equator (i.e., the middle height of the VAWT  
318 blades) is located at  $z_{eq} = 100$ m above the ground. The VAWT rotates with a fixed TSR of  
319  $\lambda = R\Omega/U_{ref}$ , where  $U_{ref}$  is the average of the instantaneous wind velocity sampled along the  
320 center line at  $1D$  upstream of the VAWT rotor region. In the current LES, the precursor simulation  
321 domain has a size of  $(L_x^p, L_y, L_z) = (2400, 2400, 400)$ m and the main turbine simulation domain  
322 has a size of  $(L_x, L_y, L_z) = (1600, 2400, 400)$ m =  $(32D, 48D, 8D)$  (including a fringe zone of  $4D$   
323 long). The precursor and main turbine simulation domains are discretized using  $384 \times 384 \times 385$   
324 and  $256 \times 384 \times 385$  grid points, respectively. The bottom boundary is flat and has a surface  
325 roughness of  $z_0 = 0.1$ m. In the precursor simulation, the ABL flow is driven by a prescribed  
326 streamwise pressure gradient as shown in Eq. (3), and the corresponding wind friction velocity is  
327  $u_* = \sqrt{-(L_z/\rho)dp_\infty/dx} = 0.52$ m/s. The mean wind speed at the turbine equator height is about  
328  $U_{eq} = 9.49$ m/s. The width of the Gaussian kernel for the ALM is set to be  $\varepsilon = 6.25$ m for the  
329 VAWT blades.

330 Note that the main simulation domain used in Shamsoddin and Porté-Agel<sup>38</sup> has a size of  
331  $(L_x, L_y, L_z) = (1200, 600, 400)$ m =  $(24D, 12D, 8D)$ , with only one VAWT included in this domain.  
332 As illustrated in Fig. 2, the ABL turbulence exhibits low- and high-speed streaks at different span-  
333 wise locations that can affect its interaction with the VAWT. If a narrow simulation domain is used,  
334 the single VAWT included in the simulation may operate in a low-speed streak for a considerable  
335 amount of time before the inflow evolves into a high-speed streak. As a result, a long simulation  
336 duration is required to obtain flow field samples for time average in order to eliminate the poten-  
337 tial bias caused by the low- and high-speed streaks. In Shamsoddin and Porté-Agel,<sup>38</sup> the total  
338 physical time of the simulation was 90.4 minutes and the sampling time span for time average was  
339 77.5 minutes. By contrast, the current LES uses a wider domain of  $L_y = 2400$ m, which allows  
340 four VAWTs to be included in the LES. The four VAWTs are located at  $x_0 = 200$ m =  $4D$  from the  
341 inflow boundary of the turbine simulation domain and are evenly spaced in the spanwise direction  
342 with a distance of  $s_y = 600$ m =  $12D$ . The ensemble average of the four VAWT sub-domains helps

## LES of Helical and Straight VAWTs in Boundary Layer Turbulence

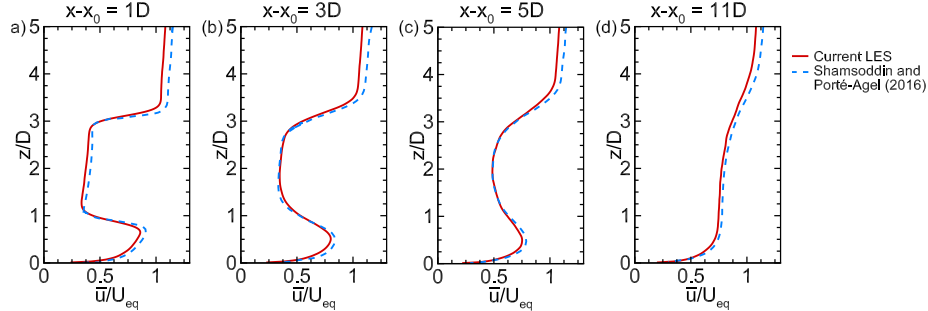


FIG. 5. Vertical profiles of mean streamwise velocity along the center line of the turbine wake at different downstream locations  $x - x_0 =$ : (a)  $1D$ ; (b)  $3D$ ; (c)  $5D$ ; and (d)  $11D$ . The results obtained from the current LES study are shown by the red solid lines, and those from Ref. [38] are shown by the blue dashed lines.

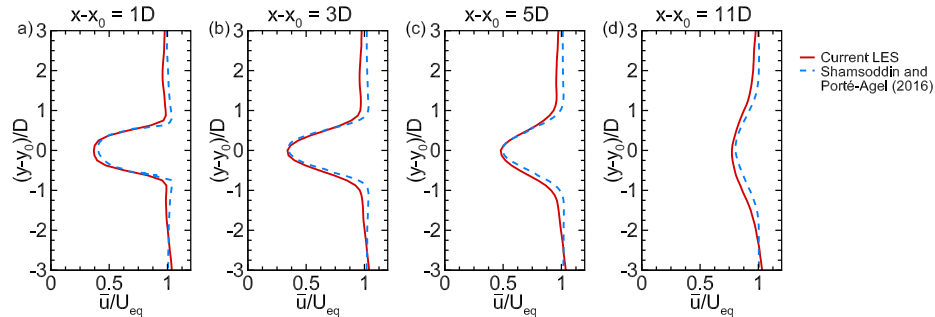


FIG. 6. Spanwise profiles of mean streamwise velocity at the equator height at different downstream locations  $x - x_0 =$ : (a)  $1D$ , (b)  $3D$ , (c)  $5D$ , and (d)  $11D$ . The results obtained from the current LES study are shown by the red solid lines, and those from Ref. [38] are shown by the blue dashed lines.

343 to obtain converged statistics with less simulation and sampling time required.

344 In the current LES test, the fully developed ABL turbulence initial condition was obtained  
 345 by running the precursor simulation without the turbine simulation domain. The precursor LES  
 346 was initialized based on the logarithmic mean velocity profile  $U(z) = (u_*/\kappa) \ln(z/z_0)$  and random  
 347 velocity fluctuations, where the von Kármán constant was set to be the typical value of  $\kappa = 0.41$ .  
 348 Note that it can be computationally expensive to run the LES at high grid resolution from the  
 349 initial random fluctuation state to the fully developed boundary layer turbulence state. To reduce  
 350 the computational cost, the grid resolution of the LES was increased successively in three stages..  
 351 The LES started at a low resolution with  $128 \times 128 \times 129$  grid points and ran for 14400s with  
 352 a time step of  $\Delta t = 0.1s$ . Then the simulation was interpolated to an intermediate resolution

## LES of Helical and Straight VAWTs in Boundary Layer Turbulence

353 with  $256 \times 256 \times 257$  grid points and was run for 4800s with a time step of  $\Delta t = 0.05$ s. After  
354 that, the simulation was interpolated to the high resolution with  $384 \times 384 \times 385$  grid points and  
355 was run for 800s with a time step of  $\Delta t = 0.016$ s. After these three stages, the fully developed  
356 ABL turbulence was obtained and was also used to initialize the turbine simulation domain in the  
357 concurrent simulation. Finally, the concurrent precursor–main simulation was conducted using  
358  $384 \times 384 \times 385$  points for the precursor simulation domain and  $256 \times 384 \times 385$  points for the  
359 main simulation domain (i.e., with identical grid resolution) for a total duration of 800s. A time  
360 average was performed over 8200 three-dimensional instantaneous flow fields sampled within the  
361 last 648s of the concurrent simulation with a time interval of about 0.079s between each sample.  
362 The corresponding dimensionless values (i.e., normalized by  $D/U_{eq}$ ) of the sampling duration and  
363 time interval are 123 and 0.015, respectively. Furthermore, as described previously, an ensemble  
364 average across the four simulated turbines was also performed. Hereinafter, the time- and turbine-  
365 averaged value of a physical quantity  $f$  is referred to as its "mean" value and denoted as  $\bar{f}$ .

366 Figures 5 and 6 show the vertical and spanwise profiles of the mean streamwise velocity at four  
367 different downstream locations of the turbine wake. The rotating VAWTs generate a significant  
368 velocity deficit in the near-wake region, which recovers gradually towards the downstream direc-  
369 tion due to the turbulent mixing. The mean velocity profiles obtained from the current LES mode  
370 show good agreement with the results reported Ref. [38], indicating that the current LES model  
371 captures the interaction of the straight-bladed VAWT with the ABL wind turbulence correctly.

## 372 IV. LES OF HELICAL-SHAPED VAWT IN BOUNDARY LAYER TURBULENCE

### 373 A. Setup of LES cases

374 In this section, we apply the LES model to simulate the effect of helical-shaped blades on the  
375 wake flow characteristics of VAWTs operating in boundary layer turbulence. One straight-bladed  
376 VAWT and two helical-bladed VAWTs are considered in order to investigate the effects of helical  
377 blade shape on the wake flow characteristics. All three VAWTs have identical key parameters  
378 except for the blade shape. In particular, each VAWT consists of three blades with the cross-  
379 sectional shape of the NACA0018 airfoil. Each blade has a vertical height of  $H = 3.2$ m and a  
380 chord length of  $c = 0.511$ m. The turbine rotor diameter is  $D = 2R = 1.8$ m, and the rotor equator  
381 is at  $z_{eq} = 8.2$ m above the ground (i.e.,  $z_{eq}/D \approx 4.56$ ). In the LES, all three VAWT models rotate

## LES of Helical and Straight VAWTs in Boundary Layer Turbulence

382 counterclockwise at the same fixed TSR of  $\lambda = R\Omega/U_{ref} = 1.19$ . For a helical-shaped VAWT,  
 383 taking the top end as the reference, if the blades are twisted counterclockwise (i.e., in the same  
 384 direction as the turbine rotation direction) towards the bottom end, the twisting angle  $\gamma$  between  
 385 the top and bottom edges is defined to be positive. In this study, two helical-bladed VAWTs with  
 386 opposite twisting angles  $\gamma = \pm 127^\circ$  are considered. The corresponding blade twist rate is  $39.69^\circ$   
 387 per meter height. Note that the  $\gamma = -127^\circ$  helical-bladed VAWT considered in the current LES  
 388 study is analogous to the commercial VAWT studied by Wei *et al.*,<sup>22</sup> except that the orientation  
 389 and direction of rotation of the turbine are both mirrored, and the cross-sectional profile of the  
 390 blades do not match precisely. The commercial helical-bladed VAWT does not use a standard  
 391 cross-sectional aerodynamic profile, and thus the lift and drag coefficients are not available for  
 392 modeling purposes. Nevertheless, the effects of the VAWT helical geometry on the wake flow  
 393 characteristics are expected to be similar despite the difference in the blade cross-sectional profile.

394 For the LES cases reported in this section, the precursor simulation domain has a size of  
 395  $(L_x^p, L_y, L_z) = (80, 80, 20)$  m and the main turbine simulation domain has a size of  $(L_x, L_y, L_z) =$   
 396  $(60, 80, 20)$  m =  $(33.33D, 44.44D, 11.11D)$  (including a fringe zone of  $4.167D$  long, i.e.,  $1/8$  of  
 397 the total domain length). The precursor and main turbine simulation domains are discretized us-  
 398 ing  $512 \times 512 \times 289$  and  $384 \times 512 \times 289$  grid points, respectively. The bottom boundary surface  
 399 roughness is  $z_0 = 0.01$  m. In the precursor simulation, the boundary layer turbulence is driven by a  
 400 prescribed streamwise pressure gradient as shown in Eq. (3), and the corresponding wind friction  
 401 velocity is  $u_* = 0.64$  m/s. The inflow and initial conditions are also generated using a similar strat-  
 402 egy as that used for the ABL condition validation case reported in Sec. III B. The mean wind speed  
 403 at the turbine equator height obtained from the precursor simulation is about  $U_{eq} = 11.79$  m/s. As  
 404 in the ABL condition validation case shown in Sec. III B, in each simulation case there are four  
 405 identical VAWTs included in the main turbine simulation domain at  $x_0 = 7.2$  m =  $4D$ , with an even  
 406 spanwise spacing of  $s_y = 20$  m =  $11.11D$ . The width of the Gaussian kernel for the ALM is set to  
 407 be  $\varepsilon = 0.16$  m for the VAWT blades.

408 The LES started at a low resolution with  $64 \times 64 \times 97$  grid points and ran for 2750 s with a  
 409 time step of  $\Delta t = 4 \times 10^{-3}$  s. Then the simulation was interpolated to an intermediate resolution  
 410 with  $256 \times 256 \times 193$  grid points and ran for 370 s with a time step of  $\Delta t = 2 \times 10^{-3}$  s. After  
 411 that, the simulation was interpolated to the high resolution with  $512 \times 512 \times 289$  grid points and  
 412 ran for another 210 s with a time step of  $\Delta t = 6.25 \times 10^{-4}$  s. After these three stages, the fully  
 413 developed boundary layer turbulence was obtained and used to also initialize the turbine simulation

## LES of Helical and Straight VAWTs in Boundary Layer Turbulence

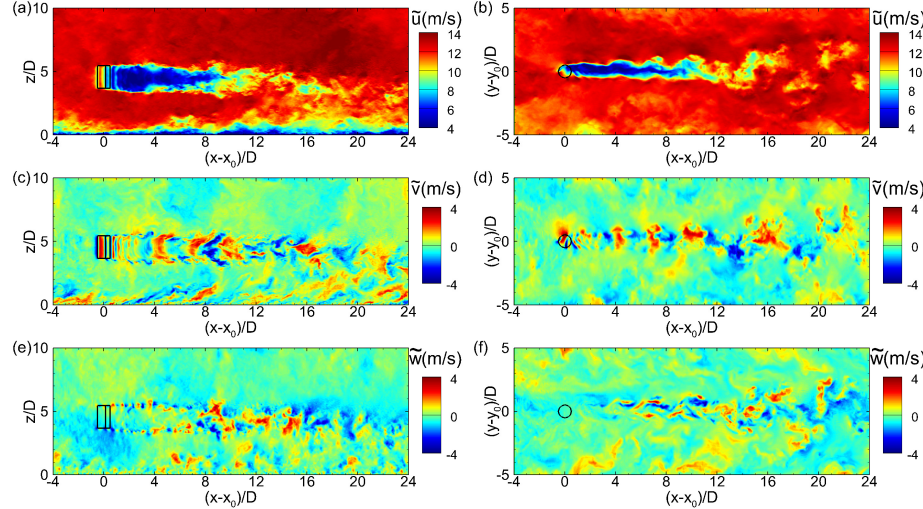


FIG. 7. Instantaneous velocity fields in boundary layer turbulence around the straight-bladed VAWT: (a,b) streamwise velocity  $\tilde{u}$ ; (c,d) spanwise velocity  $\tilde{v}$ ; (e,f) vertical velocity  $\tilde{w}$ . The left panels show the  $(x,z)$ -plane across the center of the VAWT, and the right panels show the  $(x,y)$ -plane at the VAWT equator height.

414 domain in the concurrent simulation. A time average was obtained across 4500 three-dimensional  
 415 instantaneous flow fields sampled within the last 56.25 s of the concurrent simulation with a time  
 416 interval of about 0.0125 s between each sample. The time-averaged flow statistics are presented  
 417 below in the subsections IV C–IV F.

### 418 B. Instantaneous flow fields

419 Figures 7–9 show the instantaneous velocity fields for the cases with the straight-bladed VAWT,  
 420  $-127^\circ$  helical-bladed VAWT, and  $127^\circ$  helical-bladed VAWT, respectively. In particular, the  $(x,z)$ -  
 421 plane across the center of one VAWT and the  $(x,y)$ -plane at its equator height are shown for each  
 422 case, with the origin of the horizontal coordinates shifted to the turbine center  $(x_0, y_0)$ . In the  
 423 straight-bladed VAWT case, the rotating blades induce periodic fluctuations to the streamwise  
 424 and spanwise velocities in vertical streak patterns in the near wake region (i.e.,  $x - x_0 \lesssim 4D$ )  
 425 [Fig. 7(a,c)]. In this near-wake region, the vertical velocity fluctuation is much more intensive  
 426 in the two distinct shear layers at the top and bottom edges of the turbine wake than near the  
 427 equator height [Fig. 7(e,f)]. Further downstream (i.e.,  $x - x_0 > 4D$ ), the blade-induced coherent

LES of Helical and Straight VAWTs in Boundary Layer Turbulence

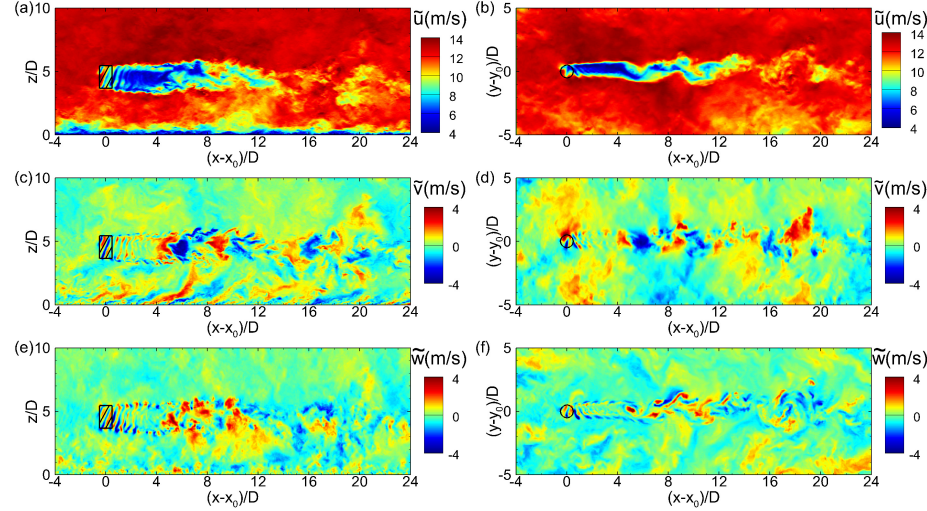


FIG. 8. Instantaneous velocity fields in boundary layer turbulence around the helical-bladed VAWT with  $\gamma = -127^\circ$ : (a,b) streamwise velocity  $\tilde{u}$ ; (c,d) spanwise velocity  $\tilde{v}$ ; (e,f) vertical velocity  $\tilde{w}$ . The left panels show the  $(x,z)$ -plane across the center of the VAWT, and the right panels show the  $(x,y)$ -plane at the VAWT equator height.

428 flow structures break down and the wake transitions to fully turbulent, as indicated by the strong  
 429 spanwise and vertical velocity fluctuations that can be seen in both the  $(x,z)$ - and  $(x,y)$ -plane views  
 430 [Fig. 7(c-f)]. The turbulent mixing associated with these fluctuations helps enhance the recovery  
 431 of the streamwise velocity as the wake flow moves downstream ( $x - x_0 \gtrsim 6D$ ).

432 The effects of the helical-shaped blades on the instantaneous velocities are more noticeable in  
 433 the near-wake region (i.e.,  $x - x_0 \lesssim 4D$ ) than in the far wake. Taking the helical-bladed VAWT with  
 434  $\gamma = -127^\circ$  as an example, the helical shape of the rotating blades causes the streak patterns of the  
 435 streamwise and spanwise velocity fluctuations to be inclined with respect to the vertical direction  
 436 [Fig. 8(a,c)]. In the near-wake region, the helical blades also induce more vertical velocity fluctua-  
 437 tions in the middle region between the top and bottom shear layers [Fig. 8(e,f)] than that in the  
 438 straight-bladed VAWT case. Moreover, a close-up look at the near-wake region in Fig. 8(f) shows  
 439 that the  $\gamma = -127^\circ$  helical blades generate downward flow motions around  $y - y_0 \approx \pm 0.5D$ , which  
 440 are accompanied by upward counter-flow motions in the middle of the wake around  $y - y_0 = 0$ .  
 441 The 3D view of this near-wake vertical flow pattern is shown in Fig. 10(b), with the straight-bladed  
 442 case shown in Fig. 10(a) for comparison. If the twisting direction of the helical blades is reversed,

LES of Helical and Straight VAWTs in Boundary Layer Turbulence

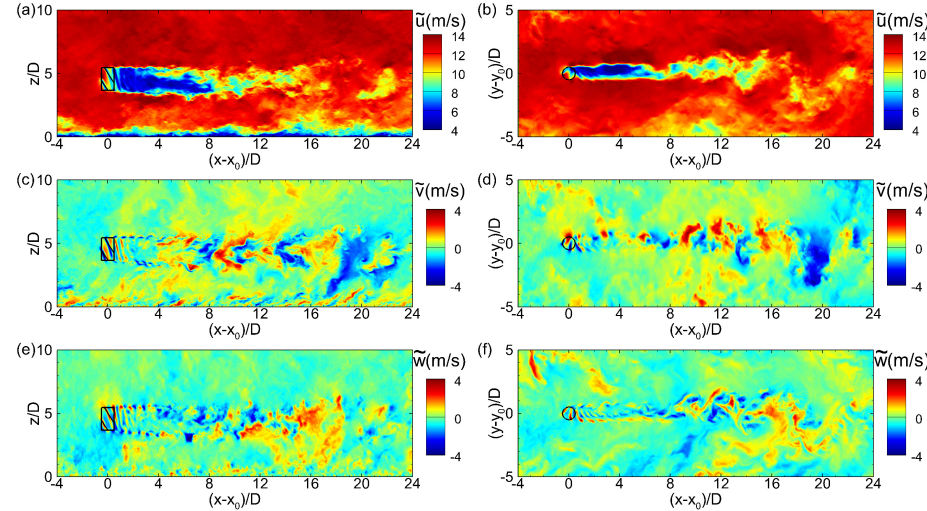


FIG. 9. Instantaneous velocity fields in boundary layer turbulence around the helical-bladed VAWT with  $\gamma = 127^\circ$ : (a,b) streamwise velocity  $\tilde{u}$ ; (c,d) spanwise velocity  $\tilde{v}$ ; (e,f) vertical velocity  $\tilde{w}$ . The left panels show the  $(x,z)$ -plane across the center of the VAWT, and the right panels show the  $(x,y)$ -plane at the VAWT equator height.

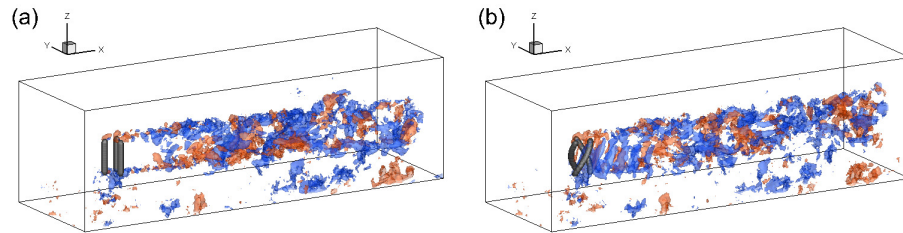


FIG. 10. Instantaneous vertical velocity fields in the wakes downstream of the (a) straight-bladed and (b) helical-bladed VAWTs with  $\gamma = -127^\circ$ . The red and blue colored iso-surfaces represent  $\tilde{w} = 1.5 \text{ m/s}$  and  $\tilde{w} = -1.5 \text{ m/s}$ , respectively. The VAWT blades are visualized using iso-surfaces (dark grey color) of the 3D Gaussian kernel (for distributing the turbine blade forces).

443 Fig. 9 shows that the  $\gamma = 127^\circ$  helical-bladed VAWT generates similar effects to the turbine wake  
 444 flow, but with the inclination direction of the streamwise and spanwise velocity fluctuations as  
 445 well as the sign of the vertical velocity fluctuations in the near-wake region reversed compared  
 446 with those in the  $\gamma = -127^\circ$  case.

### LES of Helical and Straight VAWTs in Boundary Layer Turbulence

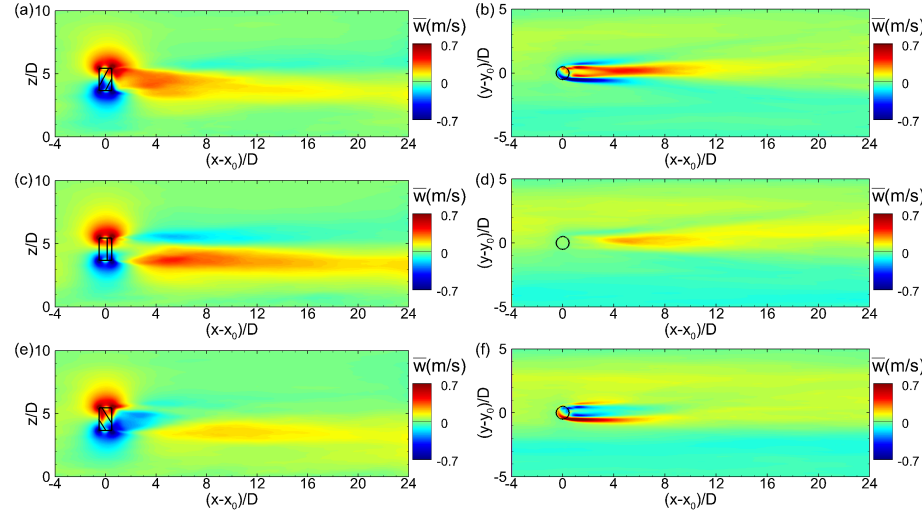


FIG. 11. Time-averaged vertical velocity  $\bar{w}$  on the  $(x,z)$ -plane across the center axis of the VAWT (left column) and on the  $(x,y)$ -plane at the equator height (right column): (a,b) helical-bladed VAWT with  $\gamma = -127^\circ$ ; (c,d) straight-bladed VAWT; (e,f) helical-bladed VAWT with  $\gamma = 127^\circ$ .

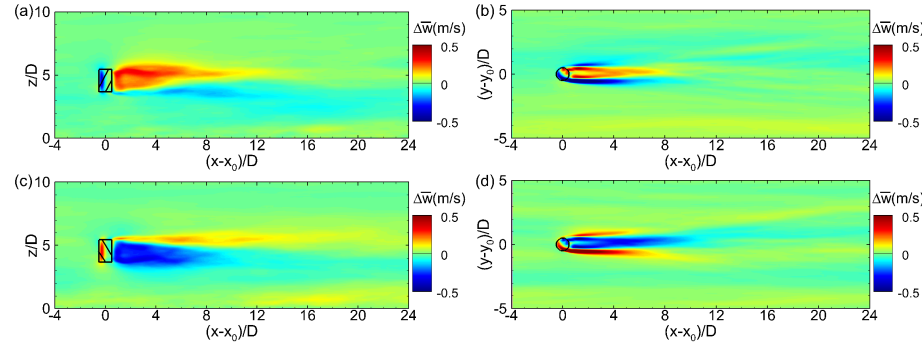


FIG. 12. Differences in the time-averaged vertical velocity relative to the straight-bladed VAWT case: (a,b) helical-bladed VAWT with  $\gamma = -127^\circ$ ; (c,d) helical-bladed VAWT with  $\gamma = 127^\circ$ .

### 447 C. Time-averaged flow fields

448 Figure 11 shows the planar views of the time-averaged vertical velocity in the wakes of the  
 449 straight- and helical-bladed VAWTs. Here, the straight-bladed VAWT case [Fig. 11(c,d)] can be  
 450 used as the baseline case to help understand the averaged effect of the helical blades on the vertical

LES of Helical and Straight VAWTs in Boundary Layer Turbulence

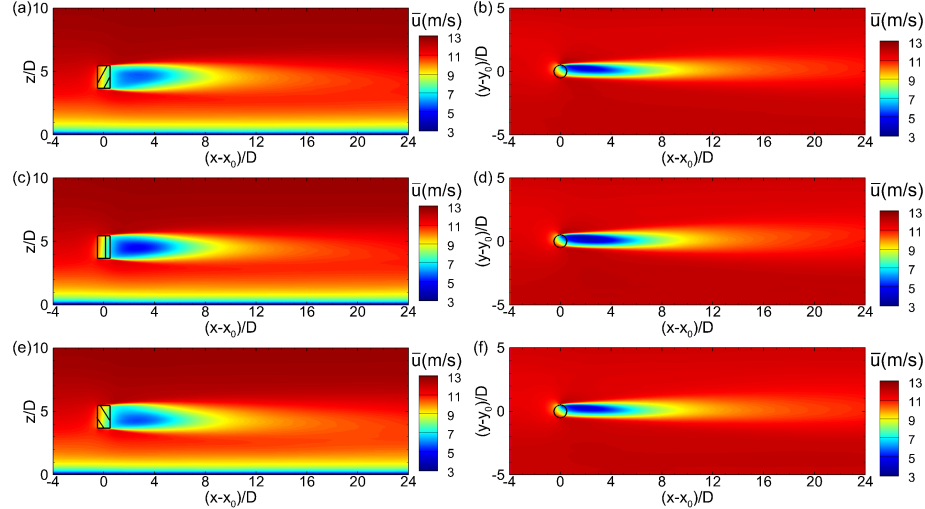


FIG. 13. Time-averaged streamwise velocity  $\bar{u}$  on the  $(x, z)$ -plane across the center axis of the VAWT (left column) and on the  $(x, y)$ -plane at the rotor equator height (right column): (a,b) helical-bladed VAWT with  $\gamma = -127^\circ$ ; (c,d) straight-bladed VAWT; (e,f) helical-bladed VAWT with  $\gamma = 127^\circ$ .

451 motions of the wake flow. As the boundary layer turbulence inflow approaches the turbine, the  
 452 blockage effect of the rotating blades forces some of the inflow to bypass the rotor, resulting  
 453 in the positive and negative  $\bar{w}$  around the top and bottom ends of the VAWT rotor, respectively  
 454 [Fig. 11(c)]. After passing the VAWT, the flow moves towards the center of the wake from top  
 455 and bottom, with the upward velocity at the bottom edge of the wake region stronger than the  
 456 downward velocity at the top edge. This net upward flow in the wake is balanced by the downward  
 457 flow next to the wake (i.e., the slightly negative  $\bar{w}$  at  $-4 \lesssim (y - y_0)/D \lesssim -1$  in Fig. 11(d)).

458 As indicated by the instantaneous flow results in Sec. IV B, the helical-shaped blades in the  
 459  $\gamma = -127^\circ$  case push the flow downwards, causing an upward counter flow to be generated at the  
 460 center of the turbine wake. This effect can also be seen clearly in Fig. 11(a,b) in the time-averaged  
 461  $\bar{w}$  field, where the two negative  $\bar{w}$  regions in the near wake correspond to the downward flows  
 462 induced directly by the forcing from the  $\gamma = -127^\circ$  helical blades and the noticeable positive  $\bar{w}$   
 463 around the center line of the near-wake region correspond to the upward counter flow. Consistent  
 464 with the instantaneous flow results, the time-averaged results for  $\bar{w}$  also show that reversing the  
 465 blade twist direction causes the blade-induced effects on the vertical flow motions to be reversed  
 466 [Fig. 11(e,f)]. To educe the net effect of the helical-shaped blades on the mean vertical motions of

LES of Helical and Straight VAWTs in Boundary Layer Turbulence

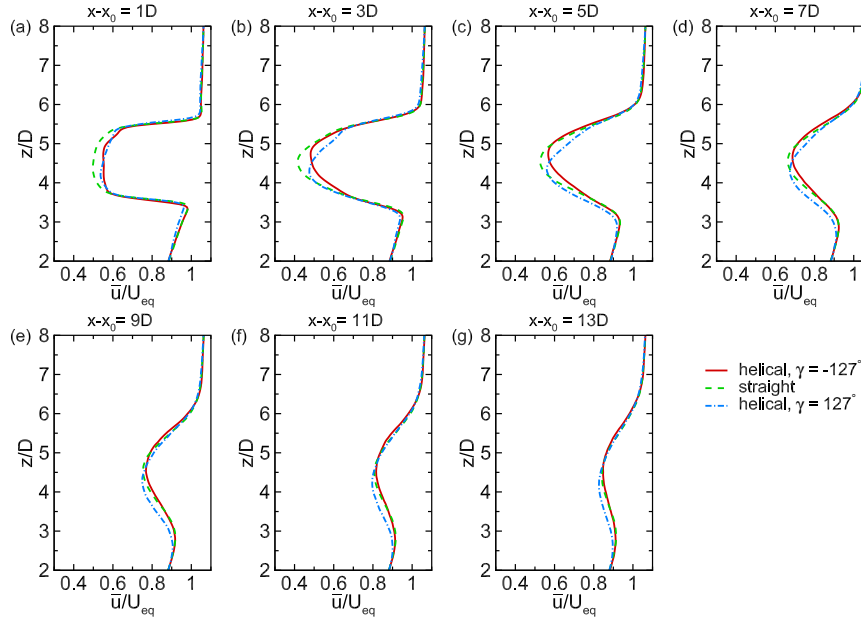


FIG. 14. Vertical profiles of  $\bar{u}$  along the wake center line at different streamwise locations ( $x - x_0$ ) =: (a) 1D; (b) 3D; (c) 5D; (d) 7D; (e) 9D; (f) 11D; (g) 13D. Solid lines: helical VAWT with  $\gamma = -127^\circ$ ; dashed lines: straight VAWT; dash-dot lines: helical VAWT with  $\gamma = 127^\circ$ .

467 the wake flow, the difference of the mean vertical velocity between the two helical-bladed VAWT  
 468 cases and the straight-bladed VAWT case are calculated. In particular, for each helical-bladed  
 469 VAWT case the difference is calculated as  $\Delta \bar{w}(x, y, z) = \bar{w}(x, y, z) - \bar{w}_s(x, y, z)$ , where  $\bar{w}_s(x, y, z)$  is  
 470 the time-averaged vertical velocity for the straight-bladed VAWT case [Fig. 11(c,d)]. As shown  
 471 in Fig. 12, the contours of  $\Delta \bar{w}$  in the wakes of the two helical-bladed VAWTs exhibit similar  
 472 magnitudes but with reversed signs. A similar effect on the mean vertical motion of the wake flow  
 473 induced by the helical-bladed VAWT has also been reported in the experimental study by Wei  
 474 *et al.*<sup>22</sup> and RANS modeling by Divakaran *et al.*<sup>28</sup>

475 Due to the mean vertical motions induced by the helical blades, the wake flow behind helical-  
 476 bladed VAWT is inclined in the vertical direction. The left column of Fig. 13 shows the 2D  
 477 contours of  $\bar{u}$  on the  $(x, z)$ -plane across the turbine center axis for the three VAWT cases, and  
 478 Fig. 14 shows the corresponding vertical profiles of  $\bar{u}$  at different streamwise locations. Compared  
 479 with the straight-bladed VAWT case, the wake of the VAWT with  $\gamma = -127^\circ$  is inclined upward

LES of Helical and Straight VAWTs in Boundary Layer Turbulence

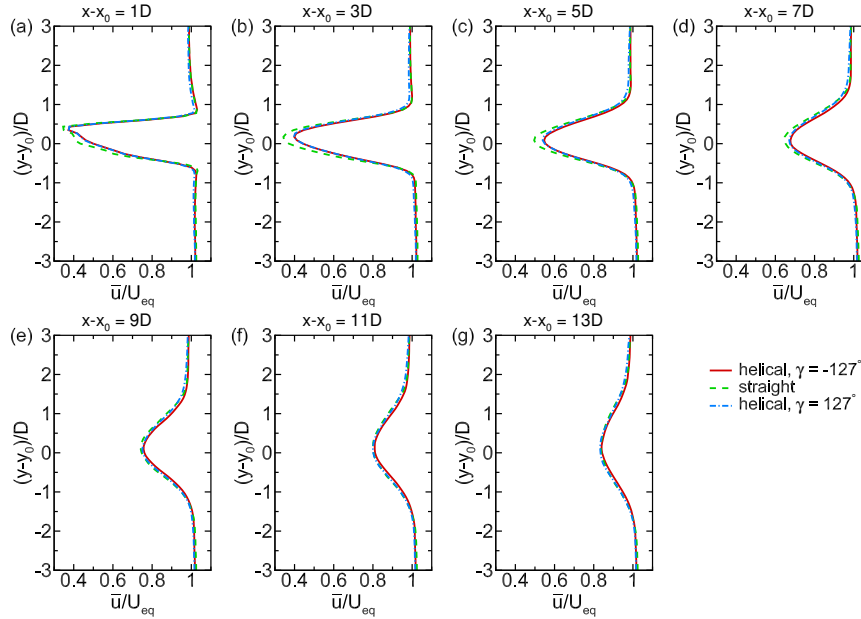


FIG. 15. Spanwise profiles of  $\bar{u}$  at the turbine equator height at different streamwise locations  $(x - x_0) =$ : (a)  $1D$ ; (b)  $3D$ ; (c)  $5D$ ; (d)  $7D$ ; (e)  $9D$ ; (f)  $11D$ ; (g)  $13D$ . Solid lines: helical-bladed VAWT with  $\gamma = -127^\circ$ ; dashed lines: straight-bladed VAWT; dash-dot lines: helical-bladed VAWT with  $\gamma = 127^\circ$ .

480 while the wake in the  $\gamma = 127^\circ$  case is inclined downward. The streamwise velocity deficits in  
 481 the two helical-bladed VAWT cases have slightly smaller magnitudes than that in the straight-  
 482 bladed VAWT case in the near-wake region  $x - x_0 \lesssim 5D$  [Fig. 14(a-c)]. The difference in the  
 483 velocity deficit becomes less significant as the wake extends further downstream. In the far wake  
 484 at  $x - x_0 \gtrsim 11D$  [Fig. 14(f,g)], the vertical profiles of  $\bar{u}$  in the straight-bladed and  $\gamma = -127^\circ$   
 485 helical-bladed VAWT cases almost overlap with each other, while  $\bar{u}$  in the  $\gamma = 127^\circ$  helical-bladed  
 486 VAWT case exhibits a slightly smaller value at  $2 \lesssim z/D \lesssim 5$ . The horizontal patterns of  $\bar{u}$  at the  
 487 equator height in the two helical-bladed VAWT cases are similar to that in the straight-bladed case  
 488 [Fig. 13(b,d,f) and Fig. 15], except for the slightly higher magnitude of streamwise velocity deficit  
 489 in the straight-bladed VAWT case in the near-wake region [Fig. 15(a-c)].

490 To quantify the effect of helical-shaped blades on the wake inclination, we define the wake

## LES of Helical and Straight VAWTs in Boundary Layer Turbulence

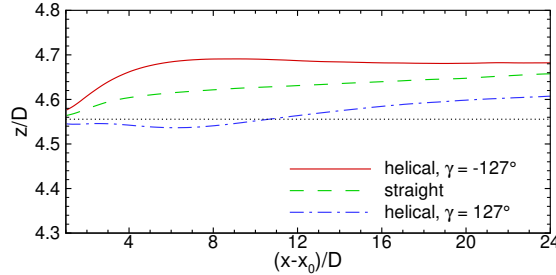


FIG. 16. Streamwise variation of turbine wake center height  $Z_c$  as defined in Eq. (19). The turbine equator height  $z_{eq}$  is also shown by the dotted line as a reference height.

491 center height at each streamwise location  $x$  as

$$492 \quad Z_c(x) = \frac{\int_{A_w} [\bar{u}(x, y, z) - \bar{u}(x_{in}, y, z)] z dA}{\int_{A_w} [\bar{u}(x, y, z) - \bar{u}(x_{in}, y, z)] dA}, \quad (19)$$

493 where  $\bar{u}(x_{in}, y, z)$  is the time-averaged streamwise velocity at the inlet  $x = x_{in}$  of the turbine simulation  
494 domain and  $A_w$  is the turbine wake cross section identified based on the condition  $\bar{u}(x, y, z) -$   
495  $\bar{u}(x_{in}, y, z) < 0$ . This definition of  $Z_c$  is analogous to that for the center of mass height of an object.  
496 Figure 16 compares  $Z_c(x)$  for the three cases. For the straight-bladed VAWT case,  $Z_c$  starts with  
497 a value that is very close to the turbine equator height  $z_{eq}$ , and increases gradually with  $x$  due  
498 to the turbulent mixing between the low-speed wake region and the high-speed free-stream wind  
499 above the wake. For comparison, the mean upward motion of the wake flow in the  $\gamma = -127^\circ$   
500 case [Fig. 12(a,b)] causes  $Z_c$  to increase much more rapidly than that in the straight-bladed VAWT  
501 case, resulting in a higher wake center height. In the  $\gamma = 127^\circ$  case, the mean downward motion  
502 of the wake flow overcomes the upward shift effect caused by the turbulent mixing between the  
503 free-stream wind and the wake flow, causing  $Z_c$  to slightly decrease and become smaller than  $z_{eq}$  at  
504  $1 \lesssim (x - x_0)/D \lesssim 10$ . At  $(x - x_0)/D > 10$ , the downward motion of the wake flow in the  $\gamma = 127^\circ$   
505 case becomes too weak [Fig. 12(c,d)], and  $Z_c$  increases to be above  $z_{eq}$  due to the effect of turbu-  
506 lent mixing. More analyses and discussions for the turbulent mixing in the turbine wake region  
507 are given in Sec. IV E.

508 Despite the vertical inclination, the magnitude of the turbine wake does not exhibit significant  
509 difference between the straight- and helical-bladed VAWT cases, suggesting that the effect of  
510 helical blades on the power production rate may be small for the flow condition and blade twist  
511 angles considered in the present study. To confirm this, the mean power coefficient for each

## LES of Helical and Straight VAWTs in Boundary Layer Turbulence

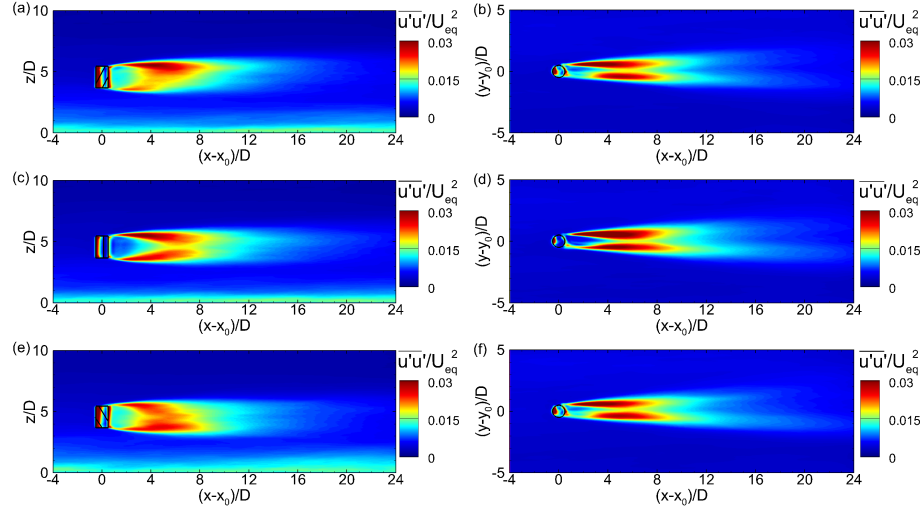


FIG. 17. Streamwise velocity variance  $\overline{u' u''}$  on the  $(x, z)$ -plane across the center axis of the VAWT (left column) and on the  $(x, y)$ -plane at the equator height (right column): (a,b) helical-bladed VAWT with  $\gamma = -127^\circ$ ; (c,d) straight-bladed VAWT; (e,f) helical-bladed VAWT with  $\gamma = 127^\circ$ .

case is calculated based on  $C_p = P/(0.5\rho H D U_{10}^3)$ , where  $P$  is the mean power (averaged in time and among the four turbines in each case) and  $U_{10}$  is the magnitude of the mean inflow velocity at 10 m reference height.<sup>22</sup> For the three cases considered here, the corresponding mean power coefficients are  $C_p = 0.0627$ ,  $0.0605$  and  $0.0622$  for  $\gamma = -127^\circ$ , straight-bladed, and  $\gamma = 127^\circ$  VAWTs, respectively. These values fall well within the range of the measured power coefficients reported in Wei *et al.*<sup>22</sup> (see their Fig. 3).

### 518 D. Time-averaged statistics of turbulent fluctuations of the VAWT wake flow

519 The LES results shown in sections IV B and IV C suggest that the helical-shaped blades can 520 affect the turbulent fluctuations in the wake flow by direct disturbance as well as by inclining the 521 wake region vertically. In this section, these effects are quantified by calculating the time-averaged 522 statistics of the VAWT wake flow.

523 Figure 17 shows the distribution of the streamwise velocity variance  $\overline{u' u''}$  on the  $(x, z)$ -plane 524 across the VAWT center and on the  $(x, y)$ -plane at the equator height. The corresponding vertical

LES of Helical and Straight VAWTs in Boundary Layer Turbulence

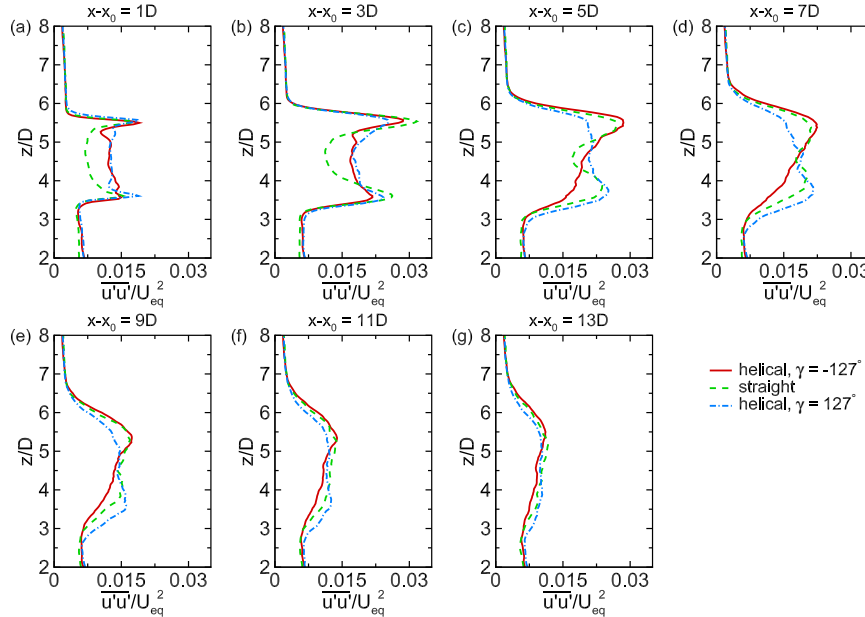


FIG. 18. Vertical profiles of  $\overline{u'u'}$  along the wake center line at different streamwise locations  $(x - x_0) =$ : (a)  $1D$ ; (b)  $3D$ ; (c)  $5D$ ; (d)  $7D$ ; (e)  $9D$ ; (f)  $11D$ ; (g)  $13D$ . Solid lines: helical-bladed VAWT with  $\gamma = -127^\circ$ ; dashed lines: straight-bladed VAWT; dash-dot lines: helical-bladed VAWT with  $\gamma = 127^\circ$ .

and spanwise profiles at various streamwise locations are shown in Figs. 18 and 19, respectively. In the straight-bladed VAWT case [Fig. 17(c,d)],  $\overline{u'u'}$  exhibits high intensity in the four shear layers extending from  $x - x_0 \approx 1D$  to  $8D$  surrounding the wake due to the shear instability, but low intensity around the middle of the wake right behind the turbine at  $1D \lesssim x - x_0 \lesssim 4D$  [Fig. 18(a,b)]. Beyond  $x - x_0 \approx 8D$ , the four shear layers merge and the magnitude of  $\overline{u'u'}$  is reduced due to turbulent dissipation. In the case of helical-bladed VAWT with  $\gamma = -127^\circ$ , the upward inclination of the wake [Fig. 13] causes the magnitude of  $\partial \overline{u} / \partial z$  to be decreased in the lower shear layer, resulting in the reduction of  $\overline{u'u'}$  there [Fig. 17(a) and Fig. 18(c-g)]. Reversing the twist angle to  $\gamma = 127^\circ$  causes the effect on  $\overline{u'u'}$  to be reversed, i.e., weakened  $\overline{u'u'}$  in the upper shear layer [Fig. 17(e) and Fig. 18(c-g)]. In both helical-bladed VAWT cases, the streamwise turbulent fluctuation is enhanced in the middle of the near-wake region (i.e., at  $1D \lesssim x - x_0 \lesssim 4D$ ) due to the direct velocity disturbance induced by the helical-shaped blades. The horizontal distribution of  $\overline{u'u'}$  is similar for the three cases [Fig. 17(b,d,e)], except that the peak values in the two horizontal

LES of Helical and Straight VAWTs in Boundary Layer Turbulence

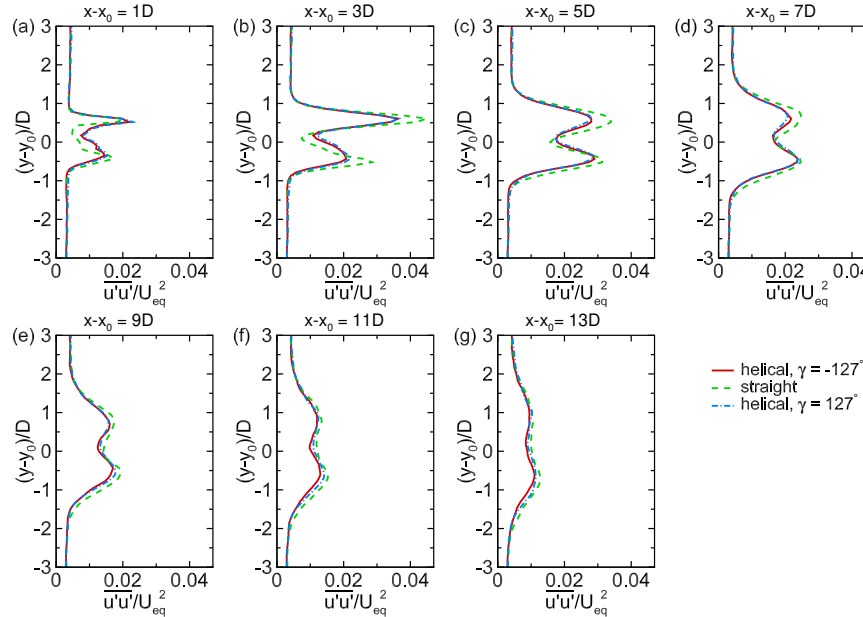


FIG. 19. Spanwise profiles of  $\overline{u'w'}$  at the turbine equator height at different streamwise locations ( $x - x_0$ ) =: (a)  $1D$ ; (b)  $3D$ ; (c)  $5D$ ; (d)  $7D$ ; (e)  $9D$ ; (f)  $11D$ ; (g)  $13D$ . Solid lines: helical-bladed VAWT with  $\gamma = -127^\circ$ ; dashed lines: straight-bladed VAWT; dash-dot lines: helical-bladed VAWT with  $\gamma = 127^\circ$ .

538 shear layers for the helical-bladed VAWT cases are slightly lower than that for the straight-bladed  
539 VAWT case [Fig. 19(b-d)].

540 Figure 20 shows the distribution of the vertical velocity variance  $\overline{w'w'}$  on the  $(x, z)$ -plane across  
541 the VAWT center and on the  $(x, y)$ -plane at the equator height. The corresponding vertical and  
542 spanwise profiles at various streamwise locations are shown in Figs. 21 and 22, respectively. Con-  
543 sistent with the direct observation of the instantaneous vertical velocity fields [Figs. 8(e,f) and  
544 9(e,f)], the helical-shaped turbine blades induce considerable vertical velocity fluctuations in the  
545 turbine-rotor region and in the near-wake region (i.e.,  $-0.5D \lesssim x - x_0 \lesssim 2D$ ) [Figs. 20, 21(a)  
546 and 22(a)]. At  $x - x_0 \gtrsim 5D$ , the upward inclination of the wake in the  $\gamma = -127^\circ$  VAWT case  
547 [Fig. 20(a)] weakens the lower shear layer, resulting in the reduction of  $\overline{w'w'}$  there. Reversing the  
548 blade twist angle to  $\gamma = 127^\circ$  causes the effect of the helical-shaped blades on  $\overline{w'w'}$  to be also  
549 reversed [Fig. 20(e)]. Unlike  $\overline{u'u'}$ , the high-intensity region of  $\overline{w'w'}$  extends over a long stream-  
550 wise distance, where the reduction of  $\overline{w'w'}$  caused by the helical-shaped blades can be observed

LES of Helical and Straight VAWTs in Boundary Layer Turbulence

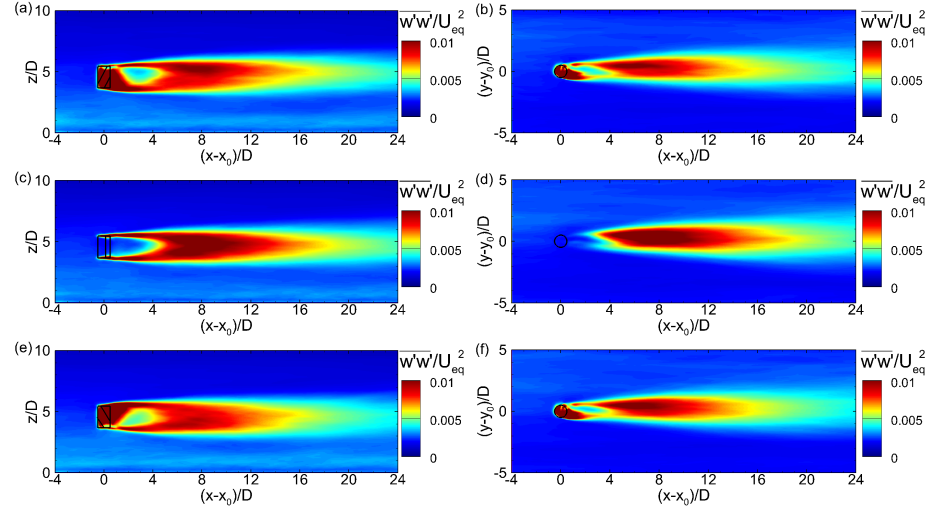


FIG. 20. Vertical velocity variance  $\overline{w'w'}$  on the  $(x,z)$ -plane across the center axis of the VAWT (left column) and on the  $(x,y)$ -plane at the equator height (right column): (a,b) helical-bladed VAWT with  $\gamma = -127^\circ$ ; (c,d) straight-bladed VAWT; (e,f) helical-bladed VAWT with  $\gamma = 127^\circ$ .

551 consistently throughout the range  $5D \lesssim x - x_0 \lesssim 13D$  [Figs. 20, 21(c–g) and 22(c–g)].

552 **E. Turbulent transport in the turbine wake**

553 The effects of the helical-shaped blades on the wake turbulence can affect the turbulence-  
554 induced mixing and transport in the wake. In this section, the statistics of the LES-resolved  
555 Reynolds stresses  $\overline{u'w'}$  and  $\overline{u'v'}$  as well as the unresolved SGS shear stresses  $\overline{\tau}_{zx}$  and  $\overline{\tau}_{yx}$  are stud-  
556 ied. In particular,  $\overline{u'w'}$  and  $\overline{\tau}_{zx}$  represent the resolved and unresolved (SGS) turbulent transport  
557 of streamwise momentum along the vertical direction, respectively;  $\overline{u'v'}$  and  $\overline{\tau}_{yx}$  represent the re-  
558 solved and unresolved (SGS) turbulent transport of streamwise momentum along the spanwise  
559 direction, respectively.

560 Figure 23 shows  $\overline{u'w'}$  (left column) and  $\overline{\tau}_{zx}$  (right column) on the  $(x,z)$ -plane across the center  
561 axis of the VAWT. Both  $\overline{u'w'}$  and  $\overline{\tau}_{zx}$  peak in the two shear layers at the upper and lower edges of  
562 the turbine wake region, with opposite signs (i.e., negative in the upper and positive in the lower  
563 layers, respectively) due to the reversed  $\partial \overline{u} / \partial z$  in these two shear layers. The magnitude of  $\overline{\tau}_{zx}$   
564 is much smaller than that of  $\overline{u'w'}$ , indicating that the dynamically important turbulent flow effects

LES of Helical and Straight VAWTs in Boundary Layer Turbulence

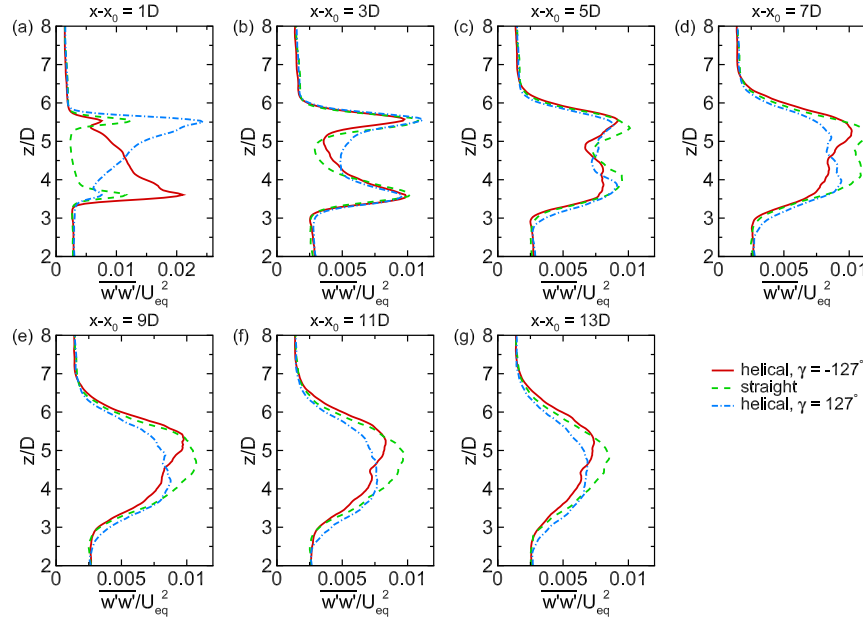


FIG. 21. Vertical profiles of  $\overline{w'w'}$  along the wake center line at different streamwise locations  $(x-x_0) =$ : (a)  $1D$ ; (b)  $3D$ ; (c)  $5D$ ; (d)  $7D$ ; (e)  $9D$ ; (f)  $11D$ ; (g)  $13D$ . Solid lines: helical-bladed VAWT with  $\gamma = -127^\circ$ ; dashed lines: straight-bladed VAWT; dash-dot lines: helical-bladed VAWT with  $\gamma = 127^\circ$ .

565 have been well resolved in the current LES. Figure 24 shows the corresponding vertical profiles  
 566 of  $\overline{u'w'}$ . The comparison between Figs. 23(a) and 23(c) shows that the magnitude of  $\overline{u'w'}$  in the  
 567 lower shear layer behind the helical-bladed VAWT with  $\gamma = -127^\circ$  is noticeably smaller than that  
 568 in the case with straight-bladed VAWT. This effect can also be seen clearly in Fig. 24(c–e).  
 569 Conversely, reversing the blade twist angle to  $\gamma = 127^\circ$  causes the weakening of  $\overline{u'w'}$  in the upper  
 570 shear layer of the wake compared with that in the straight-bladed case [Figs. 23(e) and 24(c–e)].  
 571 In the far-wake region at  $x-x_0 \gtrsim 11D$ , the difference in  $\overline{u'w'}$  among the three cases becomes  
 572 insignificant [Fig. 24(f,g)].

573 Figure 25 shows  $\overline{u'v'}$  (left column) and  $\overline{\tau}_{yx}$  (right column) on the  $(x,y)$ -plane at the turbine  
 574 equator height, and Fig. 26 shows the corresponding spanwise profiles of  $\overline{u'v'}$  at various streamwise  
 575 locations. Both  $\overline{u'v'}$  and  $\overline{\tau}_{yx}$  peak in the two shear layers at the lateral edges of the turbine wake  
 576 region, with opposite signs due to the reversed  $\partial \bar{u} / \partial y$  in these two shear layers. Similar to  $\overline{\tau}_{zx}$ ,  
 577 the magnitude of  $\overline{\tau}_{yx}$  is also much smaller than that of  $\overline{u'v'}$ . The effect of helical-shaped blades on

## LES of Helical and Straight VAWTs in Boundary Layer Turbulence

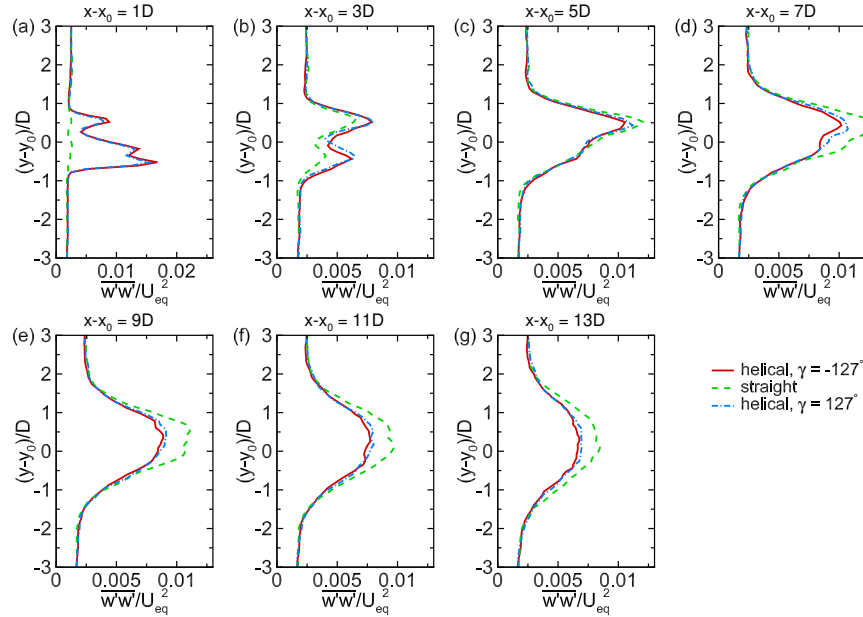


FIG. 22. Spanwise profiles of  $\overline{w'w'}$  at the turbine equator height at different streamwise locations ( $x-x_0$ ) =: (a)  $1D$ ; (b)  $3D$ ; (c)  $5D$ ; (d)  $7D$ ; (e)  $9D$ ; (f)  $11D$ ; (g)  $13D$ . Solid lines: helical-bladed VAWT with  $\gamma = -127^\circ$ ; dashed lines: straight-bladed VAWT; dash-dot lines: helical-bladed VAWT with  $\gamma = 127^\circ$ .

578  $\overline{u'v'}$  is less significant than on  $\overline{u'w'}$ , suggesting the importance of the helical blade-induced vertical  
579 inclination on the wake turbulence characteristics.

### 580 F. VAWT wake visualization based on the transport-tube method

581 The mass-flux based stream tube<sup>72,73</sup> has been widely used as a useful tool for flow analysis  
582 and visualization. Meyers and Meneveau<sup>74</sup> further generalized this transport-tube concept and ex-  
583 tended it to the visualization of momentum and energy transports. Here, this generalized transport  
584 tube method is applied to visualize the downstream development of the VAWT wakes.

585 The mean-flow stream tube can be easily constructed based on the time-averaged flow velocity  
586 vector field. For the kinetic energy transport tube, the steady-state transport equation for the mean-  
587 flow kinetic energy ( $K = \bar{u}_i \bar{u}_i / 2$ ) in the VAWT wake can be written in the index-notation form as<sup>74</sup>

## LES of Helical and Straight VAWTs in Boundary Layer Turbulence

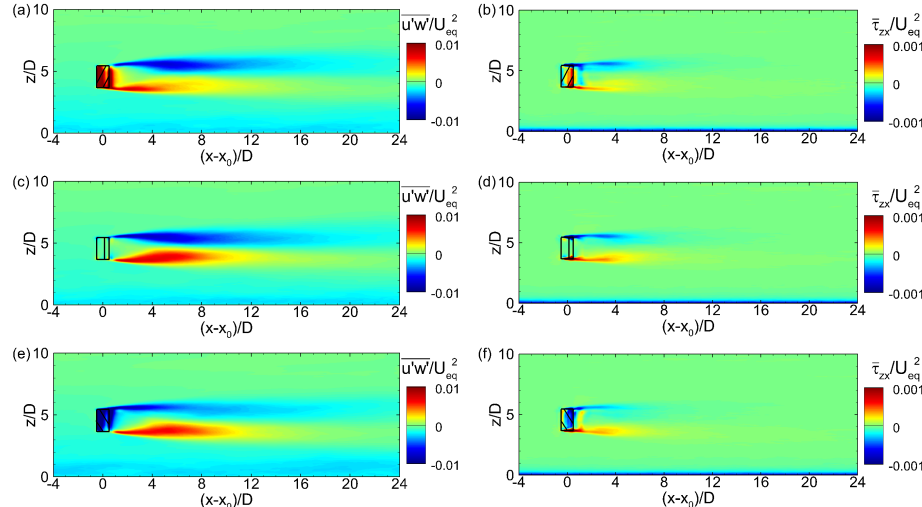


FIG. 23. Time-averaged Reynolds stress  $\overline{u'w'}$  (left column) and SGS stress  $\overline{\tau}_{zx}$  (right column) on the  $(x, z)$ -plane across the center axis of the VAWT: (a,b) helical-bladed VAWT with  $\gamma = -127^\circ$ ; (c,d) straight-bladed VAWT; (e,f) helical-bladed VAWT with  $\gamma = 127^\circ$ .

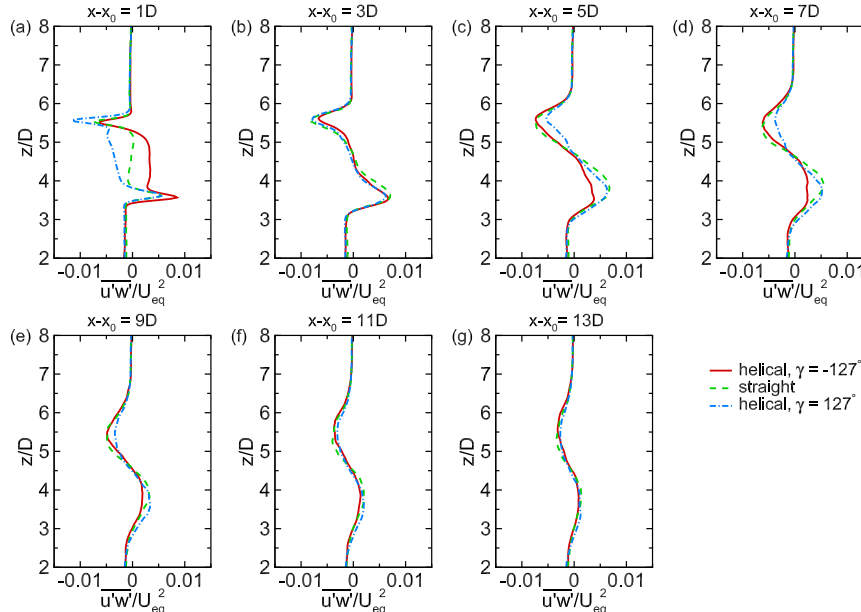


FIG. 24. Vertical profiles of  $\overline{u'w'}$  along the wake center line at different streamwise locations  $(x - x_0) =$ : (a)  $1D$ ; (b)  $3D$ ; (c)  $5D$ ; (d)  $7D$ ; (e)  $9D$ ; (f)  $11D$ ; (g)  $13D$ . Solid lines: helical-bladed VAWT with  $\gamma = -127^\circ$ ; dashed lines: straight-bladed VAWT; dash-dot lines: helical-bladed VAWT with  $\gamma = 127^\circ$ .

LES of Helical and Straight VAWTs in Boundary Layer Turbulence

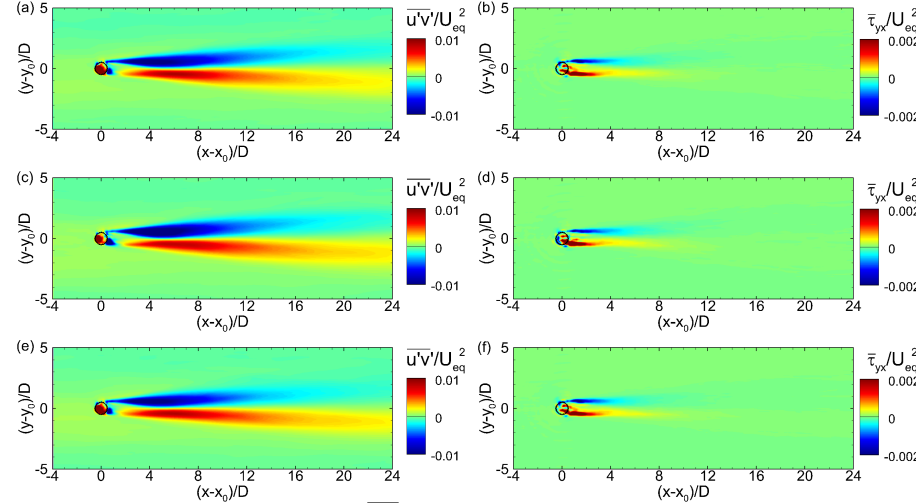


FIG. 25. Time-averaged Reynolds stress  $\overline{u'v'}$  (left column) and SGS stress  $\overline{\tau}_{yx}$  (right column) on the  $(x, y)$ -plane at the equator height of the VAWT: (a,b) helical-bladed VAWT with  $\gamma = -127^\circ$ ; (c,d) straight-bladed VAWT; (e,f) helical-bladed VAWT with  $\gamma = 127^\circ$ .

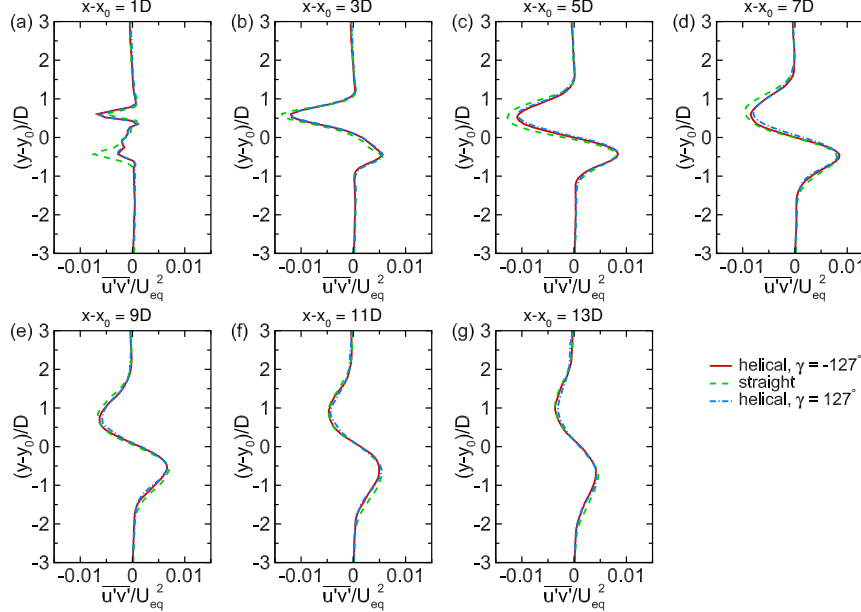


FIG. 26. Spanwise profiles of  $\overline{u'v'}$  at the turbine equator height at different streamwise locations  $(x - x_0) =$ : (a)  $1D$ ; (b)  $3D$ ; (c)  $5D$ ; (d)  $7D$ ; (e)  $9D$ ; (f)  $11D$ ; (g)  $13D$ . Solid lines: helical-bladed VAWT with  $\gamma = -127^\circ$ ; dashed lines: straight-bladed VAWT; dash-dot lines: helical-bladed VAWT with  $\gamma = 127^\circ$ .

LES of Helical and Straight VAWTs in Boundary Layer Turbulence

588

$$\frac{\partial \bar{F}_{K,j}}{\partial x_j} = -\frac{1}{\rho} \frac{\partial(\bar{u}_i \bar{p})}{\partial x_i} + \bar{u}'_i \bar{u}'_j \frac{\partial \bar{u}_i}{\partial x_j} + \bar{\tau}_{ij} \bar{S}_{ij}, \quad (20)$$

590 where

591

$$\bar{F}_{K,j} = K \bar{u}_j + \bar{u}'_i \bar{u}'_j \bar{u}_i + \bar{\tau}_{ij} \bar{u}_i \quad (21)$$

592 is the mean kinetic energy flux vector field per unit mass,  $\bar{u}_i$  is the time-averaged velocity vector  
 593 field,  $\bar{u}'_i = \tilde{u}_i - \bar{u}_i$  is the velocity fluctuation,  $\tilde{u}_i$  is the LES-resolved instantaneous velocity as de-  
 594 fined in Sec. II A,  $\bar{\tau}_{ij}$  is the time-averaged SGS stress tensor, and  $\bar{S}_{ij}$  is the time-averaged strain-rate  
 595 tensor. The three terms on the right-hand side of Eq. (20) represent the pressure transport, mean-  
 596 shear induced production, and SGS dissipation of the mean kinetic energy, respectively. Among  
 597 these terms, the pressure transport is insignificant in the wake flow; the production  $\bar{u}'_i \bar{u}'_j (\partial \bar{u}_i / \partial x_j)$   
 598 acts as a sink term for  $K$  in Eq. (20), but appears as a source term (with a reversed sign) in the  
 599 transport equation of the turbulent kinetic energy; and the SGS dissipation also acts as a sink term.

600 Based on  $\bar{F}_{K,j}$ , the corresponding kinetic energy transport velocity can be calculated as<sup>74</sup>

601

$$\bar{u}_{K,j} \equiv \bar{F}_{K,j} / K = \bar{u}_j + \bar{u}'_i \bar{u}'_j \bar{u}_i / K + \bar{\tau}_{ij} \bar{u}_i / K, \quad (22)$$

602 where the three terms on the right-hand side of Eq. (22) represents the effects due to the mean-flow  
 603 advection, the resolved turbulent transport, and the unresolved SGS transport. Recall that a stream  
 604 tube for mass transport is defined as a tubular region of fluid surrounded by streamlines of mean  
 605 velocity vector field  $\bar{u}_j$ . Analogous to the stream tube concept, a transport tube of mean kinetic  
 606 energy is defined as a tubular region surrounded by the streamlines of the  $K$ -transport velocity  $\bar{u}_{K,j}$ .  
 607 As shown in Figs. 23 and 25, the magnitudes of the SGS stress  $\bar{\tau}_{ij}$  are much smaller than those of  
 608 the corresponding Reynolds stress  $\bar{u}'_i \bar{u}'_j$ . Thus, the difference between  $\bar{u}_{K,j}$  and  $\bar{u}_j$  is mainly due to  
 609 the resolved turbulent transport as shown in Eq. (22).

610 Figure 27 shows the mean-flow stream tubes for the three VAWT cases. In each case, the  
 611 stream tube is obtained by constructing streamlines from 120 seed points (evenly spaced based on  
 612 the polar angle) on the  $(y, z)$ -plane at  $x - x_0 = 1D$  along the elliptical circle

613

$$\left( \frac{y - y_0}{D/2} \right)^2 + \left( \frac{z - z_{eq}}{H/2} \right)^2 = 1. \quad (23)$$

614 For each VAWT case, the mass flow rate is conserved along the stream tube without mass fluxes  
 615 through the tube mantle. At the starting cross-section of the stream tube at  $x - x_0 = 1D$ , the flow  
 616 velocity within the tube is smaller than the free-stream velocity outside the VAWT wake. As the

LES of Helical and Straight VAWTs in Boundary Layer Turbulence

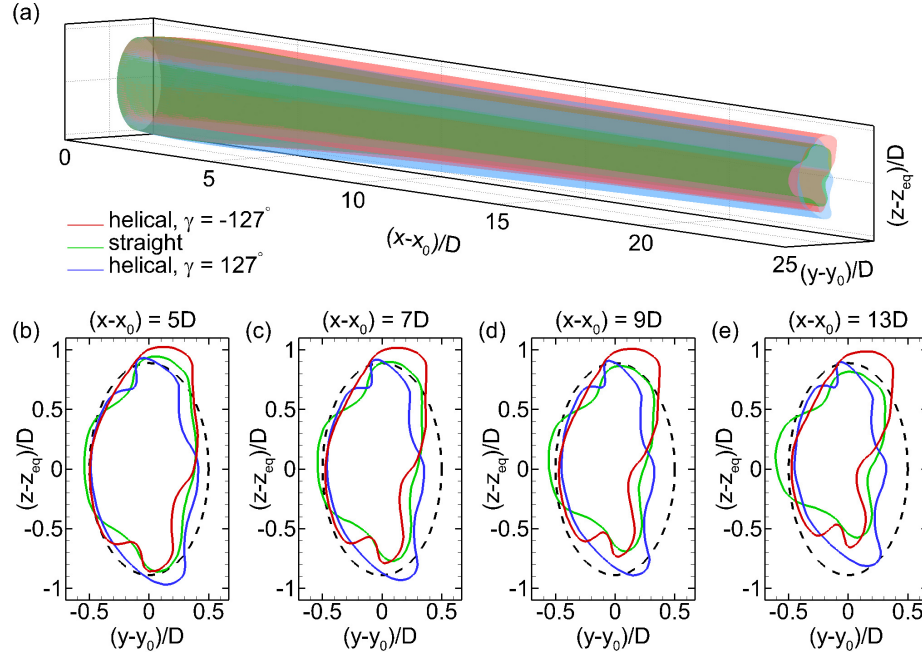


FIG. 27. Stream tubes in wake flows behind VAWTs. Panel (a) shows the three-dimensional view of the tubes: red for the helical-bladed VAWT with  $\gamma = -127^\circ$ ; green for the straight-bladed VAWT; blue for the helical-bladed VAWT with  $\gamma = 127^\circ$ . Panels (b–e) show the  $(y,z)$ -plane views of the tube mantle at four different streamwise locations, in which the dashed line indicates the prescribed initial shape of the tube cross-section at  $x - x_0 = 1D$ , and the solid color lines correspond to the three VAWT cases shown in (a).

617 wake flow moves towards the downstream direction, the stream tube cross-section shrinks as the  
 618 flow speed inside the tube recovers, and the free-stream fluid around the VAWT wake region flows  
 619 inwards to fill the space. For the straight-bladed VAWT case, the stream tube exhibits considerable  
 620 shrinkage both horizontally and vertically as it extends downstream, with the center of the tube  
 621 shifts towards  $-y$  and  $+z$  directions. By contrast, the stream tubes in the two helical-bladed  
 622 VAWT cases exhibit less shrinkage in the vertical direction than that in the straight-bladed VAWT  
 623 case. Moreover, the mean vertical velocity in the wake region induced by the helical blades [see  
 624 Figs. 11 and 12] causes the center of the stream tube to be shifted upwards in the  $\gamma = -127^\circ$  case  
 625 and downwards in the  $\gamma = 127^\circ$  case. Finally, the stream tube in the  $\gamma = 127^\circ$  case exhibits a  
 626 leftward tilt with respect to the vertical that increases with downstream distance, while the stream

LES of Helical and Straight VAWTs in Boundary Layer Turbulence

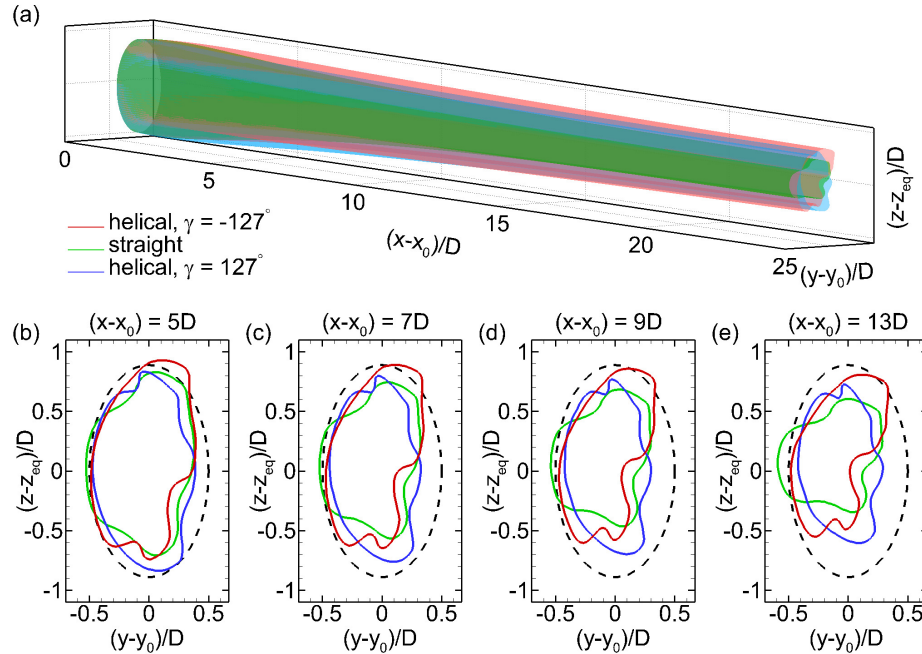


FIG. 28. Mean kinetic energy tubes in wake flows behind VAWTs. Panel (a) shows the three-dimensional view of the tubes: red for the helical-bladed VAWT with  $\gamma = -127^\circ$ ; green for the straight-bladed VAWT; blue for the helical-bladed VAWT with  $\gamma = 127^\circ$ . Panels (b–e) show the  $(y, z)$ -plane views of the tube mantle at four different streamwise locations, in which the dashed line indicates the prescribed initial shape of the tube cross-section at  $x - x_0 = 1D$ , and the solid color lines correspond to the three VAWT cases shown in (a).

627 tube in the  $\gamma = -127^\circ$  case shows an increasing rightward tilt. These behaviors were also observed  
 628 in the field experiments of Wei *et al.*<sup>22</sup>, further suggesting that the LES models in the present study  
 629 are representative of the flow phenomena around full-scale VAWTs in field conditions.

630 Figure 28 shows the mean-flow kinetic energy transport tubes constructed in a similar way as  
 631 the stream tubes shown in Fig. 27 but based on the  $K$ -transport velocity  $\bar{u}_{K,j}$  defined in Eq. (22).  
 632 Similar to the stream tubes, the kinetic energy transport tubes also exhibit shrinkage as they extend  
 633 downstream. Due to the additional effect of the resolved turbulent mixing, i.e., the second term  
 634 in Eq. (22), the shrinkage of the mean kinetic transport tube is much more significant than that of  
 635 the corresponding stream tube. Unlike the stream tube in which the mass flow rate is conserved,

## LES of Helical and Straight VAWTs in Boundary Layer Turbulence

636 the mean kinetic energy is not conserved in the wake flow along the  $K$  transport tube due to the  
637 two sink terms in Eq. (20). Nevertheless, the transport tubes visualized in Fig. 28 still possess  
638 an important property similar to the stream tube, i.e., no flux of mean kinetic energy across the  
639 tube mantles.<sup>74</sup> Taking Fig. 28(e) as an example, the difference between a specific local tube  
640 mantle at  $x - x_0 = 13D$  and the reference elliptical initial tube shape at  $x - x_0 = 1D$  provides direct  
641 visualization of how the mean kinetic energy gets entrained from the high-speed surrounding flow  
642 into the wake region to help the recovery of the wind speed. For example, the red line shown  
643 in Fig. 28(e) indicates that for the helical-bladed VAWT with  $\gamma = -127^\circ$ , the kinetic energy for  
644 recovering the mean wake flow speed is mainly from the free-stream flow on the  $+y$  and  $-z$  sides  
645 of the wake region. Overall, the stream tubes and kinetic energy transport tubes visualized in  
646 Figs. 27 and 28 show noticeable differences among the three VAWT cases, indicating that the  
647 blade geometry of the VAWT can induce considerable effects on the mass and energy transport in  
648 the turbine wake region.

## 649 V. CONCLUSIONS AND DISCUSSIONS

650 In the current work, we analyze the effect of helical blade geometry on the characteristics of  
651 VAWT wake flows based on simulation data obtained from LES. The Johns Hopkins LESGO  
652 model is adopted to simulate the atmospheric boundary layer turbulence, in which the effect of the  
653 VAWT on the wind is modeled using the ALM. Using this LES model, the turbulent wake flows  
654 behind two representative helical-bladed VAWTs with opposite blade twist angles ( $\gamma = \pm 127^\circ$ )  
655 are simulated and analyzed. One additional case based on a straight-bladed VAWT with identical  
656 key parameters as the helical-bladed VAWTs is also simulated and used as a reference case.

657 The effects of the helical-shaped blades on the VAWT wake flow can be observed from the  
658 instantaneous flow fields, the time-averaged statistics of the mean flow velocities, and the turbu-  
659 lent statistics. In particular, the twisted blades of the helical VAWTs are found to enhance the  
660 streamwise and vertical velocity fluctuations in the near-wake region of the turbines. The rotating  
661 helical blades also generate a secondary vertical flow motion in the wake region, which is found to  
662 affect the characteristics of the turbulent wake flow. Taking the  $\gamma = -127^\circ$  case as an example, the  
663 rotating helical blades push the flow downwards, resulting in the mean downward flow motions at  
664  $y - y_0 \approx \pm 0.5D$  and the upward counter flow at  $-0.5D < y - y_0 < 0.5D$  in the turbine wake that  
665 extends to  $x - x_0 \approx 10D$  [Figs. 11 and 12]. This means that the vertical flow inclines the turbine

## LES of Helical and Straight VAWTs in Boundary Layer Turbulence

666 wake upwards and weakens the shear  $\partial\bar{u}/\partial z$ . Consequently, the turbulent fluctuations  $\bar{u}'\bar{u}'$ ,  $\bar{w}'\bar{w}'$   
667 and  $\bar{u}'\bar{w}'$  are also weakened in the lower shear layer near the bottom of the turbine wake region.  
668 The simulation and statistical analysis results of the  $\gamma = 127^\circ$  case show that reversing the twist  
669 direction of the helical blades cause the aforementioned effects of the helical-bladed VAWT on  
670 the wake characteristics to be reversed. The wake-flow visualizations based on the transport-tube  
671 method also show considerable differences among the three VAWT cases regarding the transport  
672 of mass and kinetic energy from the surrounding free-stream flow into the turbine wake region.

673 To date, the characteristics of turbulent wake flows behind helical-bladed VAWTs have not been  
674 well understood compared to those for the straight-bladed VAWTs. As a result, there exist many  
675 different designs for helical-bladed VAWTs. More systematic studies are needed to help converge  
676 different design strategies into an optimal solution. Due to the high computational cost associated  
677 with the concurrent precursor simulation and the domain size for capturing the correct flow physics  
678 of boundary layer turbulence, in the present study only a limited number of cases are studied.  
679 Nevertheless, this work still identifies potential mechanisms that can affect momentum transfer,  
680 wake recovery, and wake topology. These insights can inform the design of VAWT farms, and  
681 the apparent dependence of these trends on blade twist angle can be leveraged to further optimize  
682 energy transfer in helical-bladed VAWT arrays. For example, a VAWT with a positive twist angle  
683 (e.g., the  $\gamma = 127^\circ$  VAWT studied in this work) can induce a downward inclination of the turbine  
684 wake and result in a noticeable reduction of the turbulent fluctuations [see e.g. Figs. 18(c–e) and  
685 21(c–e)] in the inflow of a downstream VAWT. This reduction of turbulent intensity is also more  
686 significant towards the upper end of the VAWT rotor height. As a result, the turbulence-induced  
687 fluctuations in the aerodynamic forces on the blades and the bending moment on the root of the  
688 rotor shaft may be significantly reduced, which can increase the longevity of the VAWTs used in  
689 a large wind farm.

## 690 ACKNOWLEDGMENTS

691 This research was supported by the National Science Foundation Fluid Dynamics Program  
692 under Grant No. 1804214 to DY and Grants No. 1802476 and 2038071 to JOD. NJW acknowl-  
693 edges support from the National Science Foundation Graduate Research Fellowship. MG and DY  
694 acknowledge the use of the Sabine and Carya clusters from the Research Computing Data Core  
695 (RCDC) at the University of Houston to carry out the numerical simulations and data analyses

## LES of Helical and Straight VAWTs in Boundary Layer Turbulence

<sup>696</sup> presented in this manuscript. MG and DY also thanks Vincent V. S. Laroche for his contribution  
<sup>697</sup> to the initial development of the Transport Tube visualization tool.

## <sup>698</sup> REFERENCES

<sup>699</sup> <sup>1</sup>J. F. Manwell, J. G. McGowan, and A. L. Rogers, *Wind Energy Explained*, 2nd ed. (Wiley, 2009).

<sup>700</sup> <sup>2</sup>T. Burton, N. Jenkins, D. Sharpe, and E. Bossanyi, *Wind Energy Handbook* (Wiley, 2011).

<sup>701</sup> <sup>3</sup>W. Short and N. Blair, "20% wind energy by 2030: Increasing wind energy's contribution to us  
<sup>702</sup> electricity supply," Tech. Rep. DOE/GO-102008-2567 (U.S. Department of Energy, 2008).

<sup>703</sup> <sup>4</sup>P. Jain, *Wind Energy Engineering*, 2nd ed. (McGraw Hill, 2016).

<sup>704</sup> <sup>5</sup>T. Letcher, *Wind Energy Engineering: A Handbook for Onshore and Offshore Wind Turbines*,  
<sup>705</sup> 1st ed. (Academic Press, 2017).

<sup>706</sup> <sup>6</sup>F. Porté-Agel, M. Bastankhah, and S. Shamsoddin, "Wind-turbine and wind-farm flows: A re-  
<sup>707</sup> view," *Boundary-Layer Meteorology* **174**, 1–59 (2020).

<sup>708</sup> <sup>7</sup>J. Meyers and C. Meneveau, "Optimal turbine spacing in fully developed wind farm boundary  
<sup>709</sup> layers," *Wind Energy* **15**, 305–317 (2012).

<sup>710</sup> <sup>8</sup>J. Contrell, T. Stehly, J. Johnson, J. O. Roberts, Z. Parker, G. Scott, and D. Heimiller, "Analy-  
<sup>711</sup> sis of transportation and logistics challenges affecting the deployment of larger wind turbines:  
<sup>712</sup> Summary of results," Tech. Rep. NREL/TP-5000-61063 (National Renewable Energy Labora-  
<sup>713</sup> tory, 2014).

<sup>714</sup> <sup>9</sup>J. Yang, L. Fang, D. Song, M. Su, X. Yang, L. Huang, and Y. H. Joo, "Review of control strategy  
<sup>715</sup> of large horizontal-axis wind turbines yaw system," *Wind Energy* **24**, 97–115 (2021).

<sup>716</sup> <sup>10</sup>M. Kinzel, Q. Mulligan, and J. O. Dabiri, "Energy exchange in an array of vertical-axis wind  
<sup>717</sup> turbines," *Journal of Turbulence* **13**, N38 (2012).

<sup>718</sup> <sup>11</sup>J. O. Dabiri, "Potential order-of-magnitude enhancement of wind farm power density via  
<sup>719</sup> counter-rotating vertical-axis wind turbine arrays," *Journal of Renewable and Sustainable En-  
<sup>720</sup> ergy* **3**, 043104 (2011).

<sup>721</sup> <sup>12</sup>I. D. Brownstein, N. J. Wei, and J. O. Dabiri, "Aerodynamically interacting vertical-axis wind  
<sup>722</sup> turbines: Performance enhancement and three-dimensional flow," *Energies* **12**, 2724 (2019).

<sup>723</sup> <sup>13</sup>M. Casini, "Small vertical axis wind turbines for energy efficiency of buildings," *Journal of  
<sup>724</sup> Clean Energy Technologies* **4**, 56–65 (2016).

<sup>725</sup> <sup>14</sup>S. H. Hezaveh, E. Bou-Zeid, M. W. Lohry, and L. Martinelli, "Simulation and wake analysis of

LES of Helical and Straight VAWTs in Boundary Layer Turbulence

726 a single vertical axis wind turbine," *Wind Energy* **20**, 713–730 (2017).

727 <sup>15</sup>G. Brochier, P. Fraunie, C. Beguier, and I. Paraschivoiu, "Water channel experiments of dynamic  
728 stall on darrieus wind turbine blades," *Journal of Propulsion and Power* **2**, 445–449 (1986).

729 <sup>16</sup>P. Bachant and M. Wosnik, "Performance and near-wake measurements for a vertical axis tur-  
730 bine at moderate Reynolds number," in *Proceedings of the ASME Fluids Engineering Summer  
731 Meeting*, 16575 (2013).

732 <sup>17</sup>D. B. Araya and J. O. Dabiri, "A comparison of wake measurements in motor-driven and flow-  
733 driven turbine experiments," *Experiments in Fluids* **56**, 150 (2015).

734 <sup>18</sup>M. Kinzel, D. B. Araya, and J. O. Dabiri, "Turbulence in vertical axis wind turbine canopies,"  
735 *Physics of Fluids* **27**, 115102 (2015).

736 <sup>19</sup>D. B. Araya and J. O. Dabiri, "Vertical axis wind turbine in a falling soap film," *Physics of Fluids*  
737 **27**, 091108 (2016).

738 <sup>20</sup>D. B. Araya, T. Colonius, and J. O. Dabiri, "Transition to bluff-body dynamics in the wake of  
739 vertical-axis wind turbines," *Journal of Fluid Mechanics* **813**, 346–381 (2017).

740 <sup>21</sup>S. H. Hezaveh, E. Bou-Zeid, G. Cortina, L. Martinelli, J. Dabiri, and M. Kinzel, "Increasing the  
741 power production of vertical-axis wind-turbine farms using synergistic clustering," *Boundary-  
742 Layer Meteorology* **169**, 275–296 (2018).

743 <sup>22</sup>N. J. Wei, I. D. Brownstein, J. L. Cardona, M. F. Howland, and J. O. Dabiri, "Near-wake structure  
744 of full-scale vertical-axis wind turbines," *Journal of Fluid Mechanics* **914**, A17 (2021).

745 <sup>23</sup>K. J. Ryan, F. Coletti, C. J. Elkins, J. O. Dabiri, and J. K. Eaton, "Three-dimensional flow field  
746 around and downstream of a subscale model rotating vertical axis wind turbine," *Experiments in  
747 Fluids* **57**, 38 (2016).

748 <sup>24</sup>C. Pearson, *Vertical Axis Wind Turbine Acoustics*, Ph.D. thesis, Cambridge University (2013).

749 <sup>25</sup>A. Alaimo, A. Esposito, A. Messineo, C. Orlando, and D. Tumino, "3D CFD analysis of a  
750 vertical axis wind turbine," *Energies* **8**, 3013–3033 (2015).

751 <sup>26</sup>M. Moghimi and H. Motawej, "Developed DMST model for performance analysis and para-  
752 metric evaluation of Gorlov vertical axis wind turbines," *Sustainable Energy Technologies and  
753 Assessments* **37**, 100616 (2020).

754 <sup>27</sup>Q. Cheng, X. Liu, H. S. Ji, K. C. Kim, and B. Yang, "Aerodynamic analysis of a helical vertical  
755 axis wind turbine," *Energies* **10**, 575 (2017).

756 <sup>28</sup>U. Divakaran, A. Ramesh, A. Mohammad, and R. K. Velamati, "Effect of helix angle on the  
757 performance of helical vertical axis wind turbine," *Energies* **14**, 393 (2021).

This is the author's peer reviewed, accepted manuscript. However, the online version of record will be different from this version once it has been copyedited and typeset.

PLEASE CITE THIS ARTICLE AS DOI: 10.1063/5.0100169

## LES of Helical and Straight VAWTs in Boundary Layer Turbulence

758 29 R. B. Cal, J. Lebrón, L. Castillo, H. S. Kang, and C. Meneveau, "Experimental study of the  
759 horizontally averaged flow structure in a model wind-turbine array boundary layer," *Journal of  
760 Renewable and Sustainable Energy* **2**, 013106 (2010).

761 30 M. Calaf, C. Meneveau, and J. Meyers, "Large eddy simulation study of fully developed wind-  
762 turbine array boundary layers," *Physics of Fluids* **22**, 015110 (2010).

763 31 N. Hamilton, H. Suk Kang, C. Meneveau, and R. Bayoán Cal, "Statistical analysis of kinetic  
764 energy entrainment in a model wind turbine array boundary layer," *Journal of Renewable and  
765 Sustainable Energy* **4**, 063105 (2012).

766 32 J. Bremseth and K. Duraisamy, "Computational analysis of vertical axis wind turbine arrays,"  
767 *Theoretical and Computational Fluid Dynamics* **30**, 387–401 (2016).

768 33 S. Xie, C. L. Archer, N. Ghaisas, and C. Meneveau, "Benefits of collocating vertical-axis and  
769 horizontal-axis wind turbines in large wind farms," *Wind Energy* **20**, 45–62 (2017).

770 34 S. El-Asha, L. Zhan, and G. V. Iungo, "Quantification of power losses due to wind turbine wake  
771 interactions through scada, meteorological and wind lidar data," *Wind Energy* **20**, 1823–1839  
772 (2017).

773 35 M. Calaf, M. B. Parlange, and C. Meneveau, "Large eddy simulation study of scalar transport in  
774 fully developed wind-turbine array boundary layers," *Physics of Fluids* **23**, 126603 (2011).

775 36 D. Yang, C. Meneveau, and L. Shen, "Large-eddy simulation of offshore wind farm," *Physics of  
776 Fluids* **26**, 025101 (2014).

777 37 L. A. Martínez Tossas, R. J. Stevens, and C. Meneveau, "Wind farm large-eddy simulations on  
778 very coarse grid resolutions using an actuator line model," *AIAA* **2016**, 1261 (2016).

779 38 S. Shamsoddin and F. Porté-Agel, "A large-eddy simulation study of vertical axis wind turbine  
780 wakes in the atmospheric boundary layer," *Energies* **9**, 366 (2016).

781 39 J. N. Sørensen and W. Z. Shen, "Numerical modeling of wind turbine wakes," *Journal of Fluids  
782 Engineering* **124**, 393–399 (2002).

783 40 S. Shamsoddin and F. Porté-Agel, "Large eddy simulation of vertical axis wind turbine wakes,"  
784 *Energies* **7**, 890–912 (2014).

785 41 L. A. Martínez-Tossas, M. J. Churchfield, and S. Leonardi, "Large eddy simulations of the flow  
786 past wind turbines: actuator line and disk modeling," *Wind Energy* **18**, 1047–1060 (2015).

787 42 L. A. Martínez-Tossas, M. J. Churchfield, and C. Meneveau, "A highly resolved large-eddy  
788 simulation of a wind turbine using an actuator line model with optimal body force projection,"  
789 *Journal of Physics: Conference Series* **753**, 082014 (2016).

## LES of Helical and Straight VAWTs in Boundary Layer Turbulence

790 43 H. Sarlak, T. Nishino, L. A. Martínez-Tossas, C. Meneveau, and J. N. Sørensen, "Assessment  
791 of blockage effects on the wake characteristics and power of wind turbines," *Renewable Energy*  
792 **93**, 340–352 (2016).

793 44 M. Abkar and J. O. Dabiri, "Self-similarity and flow characteristics of vertical-axis wind turbine  
794 wakes: an les study," *Journal of Turbulence* **18**, 373–389 (2017).

795 45 M. J. Churchfield, S. Schreck, L. A. Martínez-Tossas, C. Meneveau, and P. R. Spalart, "An  
796 advanced actuator line method for wind energy applications and beyond," *AIAA 2017*, 1998  
797 (2017).

798 46 V. Mendoza and A. Goude, "Wake flow simulation of a vertical axis wind turbine under the  
799 influence of wind shear," *Journal of Physics: Conference Series* **854**, 012031 (2017).

800 47 V. Mendoza, P. Bachant, C. Ferreira, and A. Goude, "Near-wake flow simulation of a vertical  
801 axis turbine using an actuator line model," *Wind Energy* **22**, 171–188 (2019).

802 48 V. Mendoza, A. Chaudhari, and A. Goude, "Performance and wake comparison of horizontal  
803 and vertical axis wind turbines under varying surface roughness conditions," *Wind Energy* **22**,  
804 458–472 (2019).

805 49 "LESGO: A parallel pseudo-spectral large-eddy simulation code," .

806 50 L. A. Martínez-Tossas, M. J. Churchfield, A. E. Yilmaz, H. Sarlak, P. L. Johnson, J. N. Sørensen,  
807 J. Meyers, and C. Meneveau, "Comparison of four large-eddy simulation research codes and  
808 effects of model coefficient and inflow turbulence in actuator-line-based wind turbine modeling,"  
809 *Journal of Renewable and Sustainable Energy* **10**, 033301 (2018).

810 51 J. Smagorinsky, "General circulation experiments with the primitive equations," *Monthly  
811 Weather Review* **91**, 99–164 (1963).

812 52 D. K. Lilly, "The Representation of Small-scale Turbulence in Numerical Simulation Experi-  
813 ments," in *Proceedings of the IBM Scientific Computing Symposium on Environmental Sciences*  
814 (1967).

815 53 C.-H. Moeng, "A large-eddy-simulation model for the study of planetary boundary-layer turbu-  
816 lence," *Journal of the Atmospheric Sciences* **41**, 2052–2062 (1984).

817 54 M. Germano, U. Piomelli, P. Moin, and W. H. Cabot, "A dynamic subgrid-scale eddy viscosity  
818 model," *Physics of Fluids* **3**, 1760–1765 (1991).

819 55 S. P. Pope, *Turbulent Flows* (Cambridge University Press, 2000).

820 56 E. Bou-Zeid, C. Meneveau, and M. Parlange, "A scale-dependent Lagrangian dynamic model  
821 for large eddy simulation of complex turbulent flows," *Physics of Fluids* **17**, 025105 (2005).

## LES of Helical and Straight VAWTs in Boundary Layer Turbulence

822 <sup>57</sup>Y. Wu and F. Porté-Agel, "Large-Eddy Simulation of Wind-Turbine Wakes: Evaluation of Tur-  
823 bine Parametrisations," *Boundary-Layer Meteorology* **138**, 345–366 (2011).

824 <sup>58</sup>D. Yang, C. Meneveau, and L. Shen, "Effect of downwind swells on offshore wind energy har-  
825 vesting – a large-eddy simulation study," *Renewable Energy* **70**, 11–23 (2014).

826 <sup>59</sup>S. Xiao and D. Yang, "Large-eddy simulation-based study of effect of swell-induced pitch mo-  
827 tion on wake-flow statistics and power extraction of offshore wind turbines," *Energies* **12**, 1246  
828 (2019).

829 <sup>60</sup>R. J. Stevens, J. Graham, and C. Meneveau, "A concurrent precursor inflow method for Large  
830 Eddy Simulations and applications to finite length wind farms," *Renewable Energy* **68**, 46–50  
831 (2014).

832 <sup>61</sup>P. Schlatter, N. Adams, and L. Kleiser, "A windowing method for periodic inflow/outflow bound-  
833 ary treatment of non-periodic flows," *Journal of Computational Physics* **206**, 505–535 (2005).

834 <sup>62</sup>S. Chester, C. Meneveau, and M. B. Parlange, "Modeling turbulent flow over fractal trees with  
835 renormalized numerical simulation," *Journal of Computational Physics* **225**, 427–448 (2007).

836 <sup>63</sup>W. J. McCroskey, "The phenomenon of dynamic stall," *Tech. Rep. 81264* (NASA, 1981).

837 <sup>64</sup>R. Gormont, "A mathematical model of unsteady aerodynamics and radial flow for application to  
838 helicopter rotors," *Tech. Rep. 72-67* (Army Air Mobility Research and Development Laboratory,  
839 1973).

840 <sup>65</sup>R. E. Sheldahl and P. C. Klimas, "Aerodynamic characteristics of seven symmetrical airfoil  
841 sections through 180-degree angle of attack for use in aerodynamic analysis of vertical axis  
842 wind turbines," *Tech. Rep. SAND-80-2114* (Sandia National Labs, 1981).

843 <sup>66</sup>P. Bachant and M. Wosnik, "Characterising the near-wake of a cross-flow turbine," *Journal of  
844 Turbulence* **16**, 392–410 (2015).

845 <sup>67</sup>S. A. Orszag and Y.-H. Pao, "Numerical computation of turbulent shear flows," *Advances in  
846 Geophysics* **18A**, 225–236 (1975).

847 <sup>68</sup>J. H. Ferziger and M. Perić, *Computational Methods for Fluid Dynamics*, 1st ed. (Springer,  
848 1996).

849 <sup>69</sup>J. Albertson and M. Parlange, "Surface length scales and shear stress: Implications for land-  
850 atmosphere interaction over complex terrain," *Water Resources Research* **35**, 2121–2132 (1999).

851 <sup>70</sup>S. A. Orszag, "Transform method for the calculation of vector-coupled sums: Application to the  
852 spectral form of the vorticity equation," *Journal of Atmospheric Science* **27**, 890–894 (1970).

853 <sup>71</sup>J. D. Albertson, *Large Eddy Simulation of Land-Atmosphere Interaction*, Ph.D. thesis, University

This is the author's peer reviewed, accepted manuscript. However, the online version of record will be different from this version once it has been copyedited and typeset.

PLEASE CITE THIS ARTICLE AS DOI: 10.1063/5.0100169

## LES of Helical and Straight VAWTs in Boundary Layer Turbulence

854 of California, Davis (1996).

855 <sup>72</sup>G. K. Batchelor, *An Introduction to Fluid Dynamics* (Cambridge University Press, 1967).

856 <sup>73</sup>J. Fay, *Introduction to Fluid Mechanics* (MIT Press, 1994).

857 <sup>74</sup>J. Meyers and C. Meneveau, "Flow visualization using momentum and energy transport tubes  
858 and applications to turbulent flow in wind farms," *Journal of Fluid Mechanics* **715**, 335–358  
859 (2013).